

Structural Analysis of a Scalar–Tensor Realization of Interacting Dark Energy

Pradosh Keshav MV^a NS Kavya^b Kenath Arun^a

^aDepartment of Physics and Electronics, CHRIST (Deemed to be University), Bengaluru 560029, India.

^bCenter for Mathematical Needs, Department of Mathematics, CHRIST (Deemed to be University), Bengaluru 560029, India.

E-mail: pradosh.keshav@res.christuniversity.in, kavya.ns@christuniversity.in, kenath.arun@christuniversity.in

Abstract. We investigate a class of interacting dark energy (IDE) models arising from density-driven spontaneous symmetry breaking in a conformally coupled scalar–tensor framework. In this construction, the dark matter–scalar interaction is dynamically activated as the cosmological density evolves, and the redshift dependence of the coupling follows a logistic profile whose steepness is determined by the local curvature of the symmetry-breaking potential. Working in the controlled adiabatic tracking regime, we implement the resulting epoch-dependent interaction in a perturbative background close to Λ CDM and confront the model with late-time cosmological data, including Planck 2018 CMB lensing reconstruction, redshift-space distortions, and Pantheon+SH0ES supernova data. We analyze realizations in which the activation index is allowed to vary and compare them with a restricted realization in which it is fixed to the canonical quadratic minimum value, thereby probing the structural role of the activation profile. We find no statistically significant preference for interaction over Λ CDM; current observations constrain the model to a hierarchical regime in which the scalar remains heavier than the Hubble scale at activation and background deformations remain perturbatively small. Allowing the activation index to vary preserves an extended degeneracy direction in parameter space, whereas fixing it removes this freedom and leads to a contraction of the allowed posterior region once geometric and growth data are combined. Our results delineate the viable parameter regime of symmetry–breaking IDE and clarify the structural distinction between microphysically motivated scalar–tensor realizations and phenomenological interacting models.

Contents

1	Introduction	1
2	Covariant Framework and Controlled Tracking Regime	3
2.1	Scalar-tensor origin and adiabatic reduction	3
2.2	Density-driven spontaneous symmetry breaking	5
2.3	Controlled perturbative Λ CDM regime	8
3	Attractor Structure and Logistic Normal Form	9
3.1	Local stability and attractor eigenvalue	10
3.2	Logistic normal form near the attractor	11
3.3	Polynomial realization and explicit attractor exponents	12
3.4	Scope beyond polynomial potentials	14
4	Emergent Effective Coupling and Logistic Activation	16
5	Methodology and Numerical Implementation	17
5.1	Model hierarchy and parameterization	17
5.2	Controlled perturbative regime and post-chain filtering	18
5.3	Linear perturbation implementation in CLASS	18
5.4	Data sets and statistical analysis	19
6	Observational Constraints and Analysis	20
6.1	Flexible six-parameter IDE model: posterior structure and null detection	20
6.2	Growth-sector phenomenology under flexible activation	23
6.3	Fixed-index realization and degeneracy compression	23
6.4	Structural implications of observational constraints	28
7	Structural Interpretation of Observational Constraints	29
7.1	Observational Position of the Scalar-Tensor Theory in Microscopic Parameter Space	29
7.2	Structural Meaning of Degeneracy Compression	30
8	Discussion	31
8.1	Implications for scalar-tensor IDE models	31
8.2	Implications for phenomenological IDE models	32
8.3	Future prospects	32
8.4	Conclusion	32
9	Acknowledgements	33

A	Early-Time Asymptotics and Adiabatic Consistency	33
A.1	Effective mass along the density-controlled trajectory	33
A.2	High-redshift asymptotics	34
A.3	Consistency over the observational window	35
B	Origin of the Background Deformation Parameter	35
B.1	From covariant dynamics to the reduced continuity equation	36
B.2	Mapping to the logistic activation profile	37
C	Declaration of Generative AI and AI-assisted technologies in the writing process	37

1 Introduction

Current observations indicate that the energy budget of the Universe is dominated by the dark sector, yet the fundamental nature of dark energy (DE) and dark matter (DM) remains unresolved. Although the Λ CDM model provides a remarkably successful phenomenological description of the expansion history and large-scale structure, it offers no microphysical explanation for either component. This limitation becomes more pronounced in light of persistent observational tensions, most notably the $\gtrsim 5\sigma$ discrepancy in the Hubble constant H_0 [1, 2] and the $2\text{--}4\sigma$ mismatch in the clustering amplitude $S_8 \equiv \sigma_8 \sqrt{\Omega_m/0.3}$ [3–5]. Although the precise statistical interpretation of these tensions depends on dataset selection and methodology, their recurrence across independent probes motivates the exploration of controlled extensions to Λ CDM. Such extensions should modify late-time dynamics while preserving the well-tested early-universe physics [6–8]. Any viable modification must therefore operate predominantly at $z \lesssim 2$, remain perturbatively stable, and avoid spoiling the tightly constrained early-universe sector.

If DE is dynamical rather than a strict cosmological constant, it is natural to describe it at low energies by a scalar degree of freedom. From an effective field theory (EFT) perspective, couplings between a scalar and matter fields are generically allowed unless forbidden by symmetry [9, 10]. For example, operators of the form $\phi \bar{\psi}\psi$ or conformal couplings that induce field-dependent masses are dimension-four and technically natural. The absence of interaction between DM and a scalar DE field therefore requires as much justification as its presence. Couplings to baryonic matter are tightly constrained by equivalence principle tests and fifth-force searches, which strongly suppress visible-sector interactions. By contrast, couplings confined to the dark sector remain comparatively unconstrained observationally. Interacting dark energy (IDE) models, therefore, represent a theoretically consistent and observationally viable possibility once DE is promoted from a fluid description to a dynamical scalar field.

Interacting dark energy models provide a framework in which energy–momentum exchange between cold dark matter (CDM) and DE arises from a covariant action [11, 12]. In microphysically motivated realizations, the interaction originates from the coupling of a scalar degree of freedom to matter through, for instance, conformal transformations or field-dependent fermion masses, rather than being introduced phenomenologically at the level of the background equations [13–15]. This distinguishes scalar–tensor IDE constructions from parametrized models in which the interaction kernel is specified as $Q \propto \rho$ with freely chosen redshift dependence

[16–18]. While such parametrizations are useful for data-driven exploration, they often fail to provide insight into the underlying dynamics of the coupling and may exhibit perturbative instabilities or strong sensitivity to prior assumptions [19, 20]. Although many scalar–tensor models generate time-dependent interactions, the functional form of this evolution is rarely analyzed from the perspective of the attractor structure governing the late-time dynamics.

In scalar–tensor realizations, this requirement is naturally satisfied. In the Einstein frame, a conformal coupling $A(\phi)$ induces a field-dependent DM mass of the form $m_{\text{DM}}(\phi) = m_0 A(\phi)$, with coupling strength $\beta(\phi)$ [11, 21]. Such field-dependent masses arise generically in ultraviolet completions, including dilaton and moduli sectors in string-inspired theories [22, 23] and Higgs-portal or hidden-sector constructions [24–27]. When the scalar evolves along a density-controlled tracking trajectory, the resulting energy exchange between DM and DE can remain perturbatively small at the background level. This preserves the expansion history while modifying the growth of structure through a time-dependent effective coupling. In this setting, the redshift dependence of the interaction is not prescribed phenomenologically but follows from the attractor structure of the scalar dynamics. The interaction history is then determined by the curvature properties of the effective potential along the cosmological solution, rather than by an externally imposed functional form.

A particularly transparent realization of such dynamical activation arises when the scalar potential exhibits spontaneous symmetry breaking (SSB) [28, 29]. In screening mechanisms such as the chameleon [30] and symmetron [31, 32] models, environmental density controls the effective scalar mass, suppressing the fifth force in high-density regions while permitting it in low-density environments. Similar density-dependent behavior also appears in $f(R)$ and scalaron theories [33, 34]. When transposed to the homogeneous cosmological background, the gradual dilution of the CDM density can likewise trigger a late-time symmetry-breaking transition. In this setting, the interaction between DM and DE is not externally imposed but emerges dynamically as the scalar field approaches the broken minimum of the effective potential. This mechanism allows a dark-sector coupling to remain suppressed throughout most of cosmic history and activate only at late times, preserving early-universe constraints while permitting controlled modifications to late-time structure growth [35–37].

In a preceding analysis [38], we constructed an explicit realization of density-triggered SSB based on a \mathbb{Z}_2 -symmetric quartic scalar potential coupled to DM through Yukawa or scalar-portal interactions. In that framework, the DM mass inherits the time dependence of the scalar’s vacuum expectation value (VEV) after symmetry breaking, generating an epoch-dependent effective coupling $\beta(a)$. We show that, in the overdamped tracking regime, a broad class of \mathbb{Z}_2 -symmetric symmetry-breaking potentials yields an activation profile whose leading-order normal form is logistic. Importantly, the steepness parameter n is not an arbitrary phenomenological choice but is determined by the local curvature structure of the scalar potential near the broken minimum. This observation suggests that the logistic form may represent the normal form of density-driven symmetry breaking in cosmological scalar–tensor systems. If the activation index n is fixed by the attractor structure of the potential rather than treated as a free parameter, the resulting interaction history becomes structurally constrained. This may reduce the model’s flexibility in fitting growth and geometric data simultaneously.

Motivated by this structural interpretation, the aim of the present work is to test whether

curvature-controlled activation of the dark-sector coupling is compatible with current cosmological observations. Working within the perturbative tracking regime, where deviations from Λ CDM remain small. We then separate amplitude effects from structural effects by comparing realizations in which the activation index n is treated as a free parameter with those in which it is fixed by the quadratic curvature class ($n = 3$). Building on [38, 39], we derive the late-time scaling of the scalar displacement near the broken minimum and implement the resulting logistic activation consistently within a scalar–tensor hierarchy. We then confront this framework with late-time observations, including Planck lensing [5], redshift-space distortion measurements (RSD) [40], and Pantheon+SH0ES supernova data [41]. This comparison isolates constraints on the interaction amplitude from constraints on the structural form of the activation profile, thereby directly testing the observational viability of the curvature properties of the underlying symmetry-breaking potential.

The remainder of this paper is structured as follows. Section 2 reviews the scalar–tensor framework and derives the background interaction structure, while Section 3 develops the linear perturbation equations in the presence of an epoch-dependent coupling. In Section 4, we analyze the symmetry-breaking dynamics and establish the emergence of the logistic normal form. Section 5 introduces the phenomenological parametrization used for numerical implementation. Observational constraints and their statistical interpretation are presented in Section 6, followed in Section 7 by a discussion of the structural implications of our findings and the phenomenon of degeneracy compression. We conclude in Section 8 with a summary of our main results and their implications for future work.

2 Covariant Framework and Controlled Tracking Regime

2.1 Scalar-tensor origin and adiabatic reduction

We consider a canonical scalar field ϕ with a standard two-derivative kinetic term, conformally coupled to the DM sector in the Einstein frame. The action is

$$S = \int d^4x \sqrt{-g} \left[\frac{M_{\text{Pl}}^2}{2} R - \frac{1}{2} g^{\mu\nu} \partial_\mu \phi \partial_\nu \phi - V(\phi) \right] + S_{\text{DM}} [A^2(\phi) g_{\mu\nu}, \Psi_{\text{DM}}], \quad (2.1)$$

where $M_{\text{Pl}} = (8\pi G)^{-1/2}$ is the reduced Planck mass and $A(\phi)$ is the conformal coupling function. Dark matter particles propagate on the Jordan-frame metric $A^2(\phi) g_{\mu\nu}$ and therefore acquire a field-dependent mass $m_{\text{DM}}(\phi) = A(\phi) m_0$ [42, 43]. The dimensionless coupling function is defined by

$$\beta(\phi) \equiv M_{\text{Pl}} \frac{d \ln A(\phi)}{d\phi}. \quad (2.2)$$

The non-conservation of the DM energy–momentum tensor follows from the variation of the matter action with respect to the Einstein-frame metric. Varying the action with respect to ϕ yields the exact scalar equation of motion,

$$\square \phi - V'(\phi) = \frac{\beta(\phi)}{M_{\text{Pl}}} T_{\text{DM}}, \quad (2.3)$$

where $T_{\text{DM}} = g_{\mu\nu} T_{\text{DM}}^{\mu\nu}$ is the trace of the DM energy–momentum tensor and a prime denotes differentiation with respect to ϕ . For non-relativistic matter, $T_{\text{DM}} = -\rho_{\text{DM}}$. Diffeomorphism invariance ensures conservation of the total energy–momentum tensor while allowing exchange between the scalar and DM sectors [19, 44].

The interaction term in Eq. (2.3) arises solely from the conformal rescaling of the metric and corresponds to the minimal realization of coupled quintessence. Although more general scalar–tensor theories may include both conformal and disformal interactions [45, 46], the conformal case captures the essential fifth-force and energy-exchange effects relevant for late-time cosmology and is sufficient for the present analysis. The canonical kinetic term ensures second-order equations of motion and avoids higher-derivative (Ostrogradsky) instabilities.

On a spatially flat Friedmann–Lemaître–Robertson–Walker (FLRW) background,

$$ds^2 = -dt^2 + a^2(t)d\vec{x}^2,$$

we assume the conformal coupling applies only to the DM sector, while baryons remain minimally coupled. The homogeneous field equations become

$$3M_{\text{Pl}}^2 H^2 = \rho_{\text{DM}} + \rho_\phi, \quad (2.4)$$

$$\dot{\rho}_{\text{DM}} + 3H\rho_{\text{DM}} = -\frac{\beta(\phi)}{M_{\text{Pl}}}\dot{\phi}\rho_{\text{DM}}, \quad (2.5)$$

$$\ddot{\phi} + 3H\dot{\phi} + V'(\phi) = \frac{\beta(\phi)}{M_{\text{Pl}}}\rho_{\text{DM}}, \quad (2.6)$$

where $\rho_\phi = \frac{1}{2}\dot{\phi}^2 + V(\phi)$ and $H \equiv \dot{a}/a$. Equations (2.4)–(2.6) are the exact homogeneous equations of the underlying coupled theory. Note that we allow for an additive constant in $V(\phi)$ such that the potential evaluated at the late-time minimum reproduces the observed DE density.

We now restrict attention to regimes in which the scalar evolves near a density-dependent minimum of the effective potential. Defining $m_{\text{eff}}^2(\phi) \equiv \partial^2 V_{\text{eff}}/\partial\phi^2|_{\phi=\phi_{\text{ad}}}$, the quantity m_{eff}^{-1} characterizes the local relaxation timescale of fluctuations about the minimum. In the strict heavy-field limit,

$$m_{\text{eff}}^2 \gg H^2, \quad (2.7)$$

the scalar relaxes to the instantaneous minimum on a timescale shorter than a Hubble time [30, 47]. More generally, even when the hierarchy is not parametrically large, a tracking regime may exist provided the effective mass squared at the minimum remains positive, thereby maintaining local stability. In this paper, the tracking approximation is used only as a late-time effective description. We discuss the regime of validity in detail in the following sections.

When the field remains close to a local minimum along the symmetry-broken branch, the evolution satisfies

$$\left| \frac{\ddot{\phi}}{3H\dot{\phi}} \right| \ll 1, \quad \left| \frac{\dot{\phi}}{H\phi} \right| \ll 1, \quad \dot{\phi}^2 \ll V(\phi), \quad (2.8)$$

which define an adiabatic tracking regime in which kinetic energy is subdominant and the field follows a slowly evolving attractor. Neglecting $\ddot{\phi}$ relative to $3H\dot{\phi}$ in Eq. (2.6) yields

$$3H\dot{\phi} + V'(\phi) = \frac{\beta(\phi)}{M_{\text{Pl}}}\rho_{\text{DM}}. \quad (2.9)$$

In the limit where $|3H\dot{\phi}| \ll |V'(\phi)|$, Eq. (2.9) reduces to the algebraic balance condition [31, 48]

$$V'(\phi_{\text{ad}}) = \frac{\beta(\phi_{\text{ad}})}{M_{\text{Pl}}} \rho_{\text{DM}}, \quad (2.10)$$

which defines a density-controlled trajectory $\phi_{\text{ad}}(\rho_{\text{DM}})$. The consistency of this adiabatic approximation is verified a posteriori in Appendix A using the full posterior samples.

This condition is equivalently obtained by minimizing the effective potential

$$V_{\text{eff}}(\phi; \rho_{\text{DM}}) = V(\phi) - \frac{\rho_{\text{DM}}}{M_{\text{Pl}}} \int^{\phi} \beta(\tilde{\phi}) d\tilde{\phi}, \quad (2.11)$$

where ρ_{DM} is treated as a slowly varying external parameter on Hubble timescales in the adiabatic regime. Indeed, $\partial V_{\text{eff}}/\partial \phi = 0$ reproduces Eq. (2.10). For constant microscopic coupling $\beta(\phi) = \beta_c$, the effective potential simplifies to

$$V_{\text{eff}}(\phi; \rho_{\text{DM}}) = V(\phi) - \frac{\beta_c}{M_{\text{Pl}}} \rho_{\text{DM}} \phi, \quad (2.12)$$

so that the ambient matter density induces a linear deformation of the scalar potential.

At this stage, no assumption has been made regarding the magnitude of the energy exchange relative to Hubble dilution. The coupled system defined by Eqs. (2.4)–(2.6) provides the starting point for the controlled perturbative analysis developed below.

2.2 Density-driven spontaneous symmetry breaking

Having established the covariant scalar–tensor framework and the conditions for adiabatic tracking, we now specialize to scalar potentials that exhibit SSB in vacuum and analyze how a finite DM density deforms the vacuum structure through Eq. (2.11). While the vacuum theory possesses a \mathbb{Z}_2 symmetry and degenerate minima, the presence of a matter density introduces an explicit symmetry-breaking deformation [49]. Because the deformation parameter varies continuously with cosmological time and no non-analyticity develops in V_{eff} , the resulting cosmological evolution corresponds to a smooth density-driven crossover rather than a thermodynamic phase transition. The dynamics are organized around a density-controlled attractor trajectory.

The simplest renormalizable \mathbb{Z}_2 -symmetric scalar potential is quartic (see [50–52]). More generally, if the scalar sector is regarded as an EFT valid below some cutoff scale, higher-dimensional operators consistent with the \mathbb{Z}_2 symmetry are expected [53]. We therefore consider the polynomial family

$$V(\phi) = -\frac{1}{2}\mu^2\phi^2 + \frac{\lambda}{2m}\phi^{2m}, \quad m \geq 2, \quad (2.13)$$

with $\mu^2 > 0$ and $\lambda > 0$. For $m = 2$ this reduces to the standard Mexican-hat potential, while $m > 2$ describes progressively flatter minima generated by higher-order operators.

The symmetric point $\phi = 0$ is unstable in vacuum. In vacuum ($\rho_{\text{DM}} = 0$), the extrema satisfy

$$-\mu^2\phi + \lambda\phi^{2m-1} = 0,$$

yielding the symmetric point $\phi = 0$ and the degenerate broken minima

$$\phi = \pm v, \quad v \equiv \left(\frac{\mu^2}{\lambda} \right)^{\frac{1}{2m-2}}, \quad (2.14)$$

which defines the VEV. The curvature at the broken minimum is

$$m_\phi^2 \equiv V''(v) = 2(m-1)\mu^2, \quad (2.15)$$

which sets the intrinsic scalar mass scale in vacuum. The vacuum value $V(v)$ is assumed to be adjusted to reproduce the observed late-time cosmological constant.

For the analytic illustration below, we specialize to a constant microscopic coupling, ($\beta(\phi) = \beta_c$), so that the effective potential (2.11) in the presence of finite matter density becomes

$$V_{\text{eff}}(\phi; \rho_{\text{DM}}) = -\frac{1}{2}\mu^2\phi^2 + \frac{\lambda}{2m}\phi^{2m} - \frac{\beta_c}{M_{\text{Pl}}}\rho_{\text{DM}}\phi, \quad (2.16)$$

where the linear term explicitly breaks the \mathbb{Z}_2 symmetry whenever $\rho_{\text{DM}} \neq 0$, lifting the vacuum degeneracy and selecting a unique global minimum. The equilibrium condition along the tracking trajectory follows from Eq. (2.10),

$$-\mu^2\phi + \lambda\phi^{2m-1} - \frac{\beta_c}{M_{\text{Pl}}}\rho_{\text{DM}} = 0. \quad (2.17)$$

For $\beta_c > 0$, the minimum lies at $\phi > 0$, selecting the branch continuously connected to the positive vacuum minimum [54]. We restrict attention to this branch throughout the paper.

To make the structure transparent, we introduce the dimensionless variables

$$x \equiv \frac{\phi_{\text{ad}}}{v}, \quad \xi(a) \equiv \frac{\beta_c \rho_{\text{DM}}(a)}{\lambda v^{2m-1} M_{\text{Pl}}}, \quad (2.18)$$

where v is defined in Eq. (2.14). Eliminating μ^2 using Eq. (2.14), the balance condition (2.17) reduces to

$$x^{2m-1} - x = \xi(a), \quad (2.19)$$

where $\xi(a)$ is a dimensionless deformation parameter that measures the strength of the density-induced tilt of the effective potential relative to the intrinsic restoring scale of the vacuum minimum. In particular, $\xi(a)$ compares the linear symmetry-breaking term $\beta_c \rho_{\text{DM}}/M_{\text{Pl}}$ to the characteristic restoring force λv^{2m-1} of the vacuum potential. Large values $|\xi| \gg 1$ correspond to epochs where the matter-induced deformation dominates over the vacuum structure, while $|\xi| \ll 1$ corresponds to the regime in which the scalar approaches its VEV.

In the regime where the energy-exchange term in Eq. (2.5) remains perturbatively small (to be quantified in Sec. 2.3), one has $\rho_{\text{DM}} \propto a^{-3}$ to good approximation [20], implying

$$\xi(a) = \xi_0 a^{-3}, \quad \xi_0 \equiv \xi(a=1).$$

Equation (2.19) therefore determines a one-dimensional density-controlled trajectory $x(a)$. At early times ($\xi \gg 1$), the highest-power term dominates and

$$x^{2m-1} \simeq \xi,$$

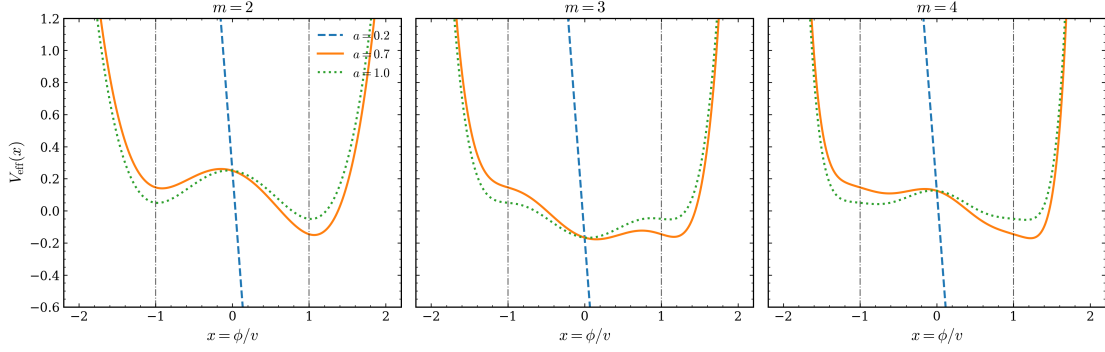


Figure 1: Dimensionless effective potential $V_{\text{eff}}(x)$ for the polynomial class (3.12) with $m = 2, 3, 4$ (left to right). Each curve shows representative epochs corresponding to decreasing deformation parameter $\xi(a) = \xi_0 a^{-3}$. At early times ($\xi \gg 1$), the density-induced linear term lifts the vacuum degeneracy and selects a unique minimum at $x > 1$. As $\xi(a)$ decreases with expansion, the deformation weakens and the minimum approaches the vacuum value $x = 1$. The progressive flattening of the minimum for larger m illustrates how the local restoring structure controls the width of the density-driven crossover.

so that

$$x(a) \sim \xi^{1/(2m-1)} \propto a^{-3/(2m-1)}.$$

Thus $x \gg 1$ at high density, corresponding to $\phi_{\text{ad}} \gg v$. In this regime the field explores the large-field region of the potential, where the curvature scales as

$$V''(\phi_{\text{ad}}) \sim \lambda(2m-1)\phi_{\text{ad}}^{2m-2}.$$

The effective mass therefore increases at high density, supporting the existence of a dynamically stable tracking branch as discussed in Eq. (2.7) over the relevant epoch.

Differentiating Eq. (2.19) with respect to $\ln a$ and using $d\xi/d\ln a = -3\xi$ yields

$$[(2m-1)x^{2m-2} - 1] \frac{dx}{d\ln a} = -3\xi(a). \quad (2.20)$$

Eliminating $\xi(a)$ via Eq. (2.19) gives the autonomous evolution equation

$$\frac{dx}{d\ln a} = \frac{3x(1-x^{2m-2})}{1-(2m-1)x^{2m-2}}. \quad (2.21)$$

For the quartic case $m = 2$, this reduces to

$$\frac{dx}{d\ln a} = \frac{3x(1-x^2)}{1-3x^2}. \quad (2.22)$$

Equation (2.21) defines the exact autonomous flow along the density-controlled tracking trajectory. Along the physical branch corresponding to $\beta_c > 0$, and for parameter values satisfying the perturbative bound, the denominator does not vanish over the cosmologically relevant redshift range. This means that on the physical branch with $x \gg 1$, the denominator remains

negative definite for $m \geq 2$, avoiding singular behavior. The trajectory evolves monotonically from $x \gg 1$ at early times toward the broken vacuum minimum $x \rightarrow 1$ at late times.

The detailed late-time stability properties of this attractor and its relation to the logistic normal form are analyzed in the following sections.

2.3 Controlled perturbative Λ CDM regime

The coupled background system defined by Eqs. (2.4)–(2.6) generically allows energy exchange between DM and the scalar field. In this section, we restrict attention to a controlled perturbative regime in which the associated energy exchange remains perturbatively small, so that the homogeneous expansion history is effectively indistinguishable from Λ CDM.

To quantify the magnitude of the interaction relative to Hubble friction, we define the dimensionless quantity

$$\varepsilon(a) \equiv \frac{\beta(\phi)\dot{\phi}}{M_{\text{Pl}}H}, \quad (2.23)$$

where $\varepsilon(a)$ measures the fractional deviation from standard a^{-3} matter dilution per Hubble time. Using Eq. (2.5), the DM continuity equation becomes

$$\dot{\rho}_{\text{DM}} + 3H\rho_{\text{DM}} = -\varepsilon(a)H\rho_{\text{DM}}. \quad (2.24)$$

In the adiabatic tracking limit, differentiating (2.10) and linearizing around the instantaneous minimum yields the approximate scaling

$$\dot{\phi} \sim -3H \frac{\beta(\phi)\rho_{\text{DM}}}{M_{\text{Pl}}m_{\text{eff}}^2}. \quad (2.25)$$

Substituting this into Eq. (2.23) gives

$$\varepsilon(a) \sim 3 \frac{\beta^2(\phi)\rho_{\text{DM}}}{M_{\text{Pl}}^2 m_{\text{eff}}^2}. \quad (2.26)$$

During matter domination, where $3M_{\text{Pl}}^2 H^2 \simeq \rho_{\text{DM}}$, this can be written transparently as

$$\varepsilon(a) \sim 3\beta^2(\phi) \frac{H^2}{m_{\text{eff}}^2}. \quad (2.27)$$

The interaction is therefore parametrically suppressed whenever either the effective mass hierarchy (2.7) holds or the microscopic coupling $\beta(\phi)$ is sufficiently small. A complete derivation of the reduced continuity equation and the relation between $\varepsilon(a)$ and the microscopic parameters is presented in Appendix B.

Equation (2.24) can be formally integrated to give

$$\rho_{\text{DM}}(a) = \rho_{\text{DM},0} a^{-3} \exp \left[- \int_{a_0}^a \varepsilon(a') d \ln a' \right]. \quad (2.28)$$

The cumulative fractional deviation from standard a^{-3} dilution is therefore controlled by

$$\Delta \ln \rho_{\text{DM}} = \int \varepsilon(a) d \ln a, \quad (2.29)$$

integrated from some initial scale factor a_i to a . If $|\varepsilon(a)| \leq \varepsilon_{\max}$ over the redshift interval of interest (typically $z \lesssim 2$, corresponding to $\Delta \ln a = \mathcal{O}(1)$), then

$$\left| \ln \frac{\rho_{\text{DM}}(a)}{\rho_{\text{DM},0} a^{-3}} \right| \leq \int |\varepsilon(a)| d \ln a \lesssim \varepsilon_{\max}. \quad (2.30)$$

Thus, the maximum instantaneous value of $|\varepsilon(a)|$ bounds the cumulative background deformation over the observationally relevant epoch.

To ensure that the homogeneous expansion remains observationally indistinguishable from Λ CDM, we impose the requirement

$$\max_a |\varepsilon(a)| < \varepsilon_*, \quad (2.31)$$

where ε_* is chosen such that the cumulative deviation in Eq. (2.28) remains below current observational sensitivity. Present background measurements [5, 55, 56] constrain the expansion history at the percent level, motivating the benchmark choice $\varepsilon_* = 10^{-2}$. This corresponds to sub-percent deviations in the matter density and Hubble rate over the redshift range probed by current data [57].

All posterior samples violating Eq. (2.31) are rejected, thereby restricting the analysis to a controlled perturbative regime. For each proposed parameter vector, $\varepsilon(a)$ is computed along the background solution over $0 \leq z \leq 5$, and the maximum value is used to enforce (2.31).

Within the regime defined by Eq. (2.31), the matter density satisfies

$$\rho_{\text{DM}}(a) = \rho_{\text{DM},0} a^{-3} [1 + \mathcal{O}(\varepsilon_*)],$$

and the Friedmann equation reduces to

$$H^2(a) = H_0^2 (\Omega_m a^{-3} + 1 - \Omega_m) + \mathcal{O}(\varepsilon_*), \quad (2.32)$$

where $1 - \Omega_m$ is supplied by the vacuum value of the scalar potential and deviations of order $\mathcal{O}(\varepsilon_*)$ are below current background sensitivity. The background expansion is therefore perturbatively equivalent to Λ CDM, while the time-dependent coupling $\beta_{\text{eff}}(a) = \beta[\phi_{\text{ad}}(a)]$ may still generate observable modifications in the growth sector.

All subsequent theoretical derivations and numerical analyses are restricted to this controlled perturbative regime.

3 Attractor Structure and Logistic Normal Form

The density-controlled trajectory defined by Eq. (2.19) evolves according to the autonomous flow equation (2.21). In this section, we analyze the local stability properties of the late-time attractor and demonstrate that its linearized dynamics are governed by a universal eigenvalue determined by the order of the first nonvanishing derivative of the scalar potential at its minimum.

3.1 Local stability and attractor eigenvalue

Consider a general scalar potential admitting a smooth (analytic) minimum at $\phi = v$. In a neighborhood of the minimum, the first derivative of the potential can be expanded as

$$V'(\phi) = \kappa_p (\phi - v)^p + \mathcal{O}((\phi - v)^{p+1}), \quad (3.1)$$

where $p \geq 1$ denotes the order of the first non-vanishing term in the expansion of $V'(\phi)$ about $(\phi = v)$, i.e., the lowest power for which the coefficient is nonzero. For $(p > 1)$, one has $(V''(v) = 0)$, so the leading restoring force is nonlinear. Stability then requires that the first non-vanishing even derivative of (V) at $(\phi = v)$ be positive [58].

Specializing for analytic clarity to a constant microscopic coupling, $\beta(\phi) = \beta_c$, the adiabatic balance condition of Eq. (2.10) reads

$$V'(\phi_{\text{ad}}) = \frac{\beta_c}{M_{\text{Pl}}} \rho_{\text{DM}}.$$

This simplification is used only to make the local scaling behavior explicit. The resulting attractor exponent depends solely on the structure of $V'(\phi)$ near the minimum and therefore extends to the general case with a time-dependent effective coupling $\beta_{\text{eff}}(a) = \beta[\phi_{\text{ad}}(a)]$.

Defining the displacement from the minimum as $\delta(a) \equiv \phi_{\text{ad}}(a) - v$ and assuming $|\delta| \ll v$ so that the local expansion (3.1) is valid, the balance equation implies to leading order

$$\kappa_p \delta^p = \frac{\beta_c}{M_{\text{Pl}}} \rho_{\text{DM}}(a) + \mathcal{O}(\delta^{p+1}). \quad (3.2)$$

In the controlled perturbative regime (c.f. Sec. 2.3), the background matter density scales as $\rho_{\text{DM}}(a) \propto a^{-3}$ to leading order. Equation (3.2) therefore implies the scaling

$$\delta(a) \propto \rho_{\text{DM}}(a)^{1/p} \propto a^{-\frac{3}{p}}. \quad (3.3)$$

Differentiating the scaling relation yields the linearized flow equation for perturbations around the minimum

$$\frac{d\delta}{d \ln a} = -\frac{3}{p} \delta + \mathcal{O}(\delta^2), \quad (3.4)$$

so that $\delta = 0$ defines a hyperbolic fixed point (see [59, 60]) of the reduced one-dimensional autonomous flow with eigenvalue

$$\lambda_p = -\frac{3}{p}. \quad (3.5)$$

The magnitude of the eigenvalue decreases as p increases, implying a progressively slower approach to the attractor for increasingly flat minima. The attractor exponent is, therefore, determined by the background dilution law $\rho_{\text{DM}} \propto a^{-3}$ and the local restoring order p of the scalar potential. Importantly, the result depends only on the local analytic structure of $V(\phi)$ near $\phi = v$ and not on its global nonlinear behavior, provided that no additional time-dependent sources or breakdown of adiabatic tracking occur.

3.2 Logistic normal form near the attractor

The previous subsection showed that the displacement from the minimum decays with eigenvalue (3.5). We now recast the late-time dynamics near the attractor in a form that makes the nonlinear structure explicit and connects naturally to parametrizations commonly used in phenomenological IDE analyses [16, 39, 61–66].

To make the structure of the late-time approach explicit, we introduce the dimensionless order parameter

$$x(a) \equiv \frac{\phi_{\text{ad}}(a)}{v}, \quad x \rightarrow 1 \quad \text{as} \quad a \rightarrow \infty,$$

where v denotes the VEV of the scalar field. Writing the displacement from the minimum as $\delta(a) \equiv \phi_{\text{ad}}(a) - v$, we have

$$x = 1 + \frac{\delta}{v},$$

so that δ/v measures the dimensionless deviation of x from unity.

From Eq. (3.4), the late-time linearized evolution of the displacement is

$$\frac{d\delta}{d\ln a} = -\frac{3}{p}\delta + \mathcal{O}(\delta^2), \quad (3.6)$$

valid in the regime $|\delta| \ll v$. This result holds within the adiabatic tracking regime, where the density evolution follows ($\rho_{\text{DM}} \propto a^{-3}$). Dividing by v and using $x = 1 + \delta/v$, this implies

$$\frac{dx}{d\ln a} = -\frac{3}{p}(x-1) + \mathcal{O}((x-1)^2). \quad (3.7)$$

It is convenient to introduce the inverse variable $y(a) \equiv 1/x(a)$. This change of variables compactifies the physical domain ($x \in [1, \infty)$) to ($y \in (0, 1]$), making the late-time fixed point appear at ($y = 1$) and facilitating comparison with standard logistic dynamics. Along the physical branch, x decreases monotonically (c.f. Eq. (2.21)) from large values at early times toward $x \rightarrow 1$ at late times, so that y evolves from $y \rightarrow 0^+$ to $y \rightarrow 1$.

Differentiating $y = 1/x$ with respect to $\ln a$ gives

$$\frac{dy}{d\ln a} = -\frac{1}{x^2} \frac{dx}{d\ln a}.$$

Substituting Eq. (3.7) and expanding around $x = 1$ (so that $1/x^2 = 1 + \mathcal{O}(x-1)$) yields

$$\frac{dy}{d\ln a} = \frac{3}{p} \frac{x-1}{x^2} + \mathcal{O}((x-1)^2) \quad (3.8)$$

$$= \frac{3}{p} (1-y)y + \mathcal{O}((1-y)^2), \quad (3.9)$$

where we used the identity

$$x-1 = \frac{1-y}{y}$$

and retaining only the leading nonlinear contribution near the stable fixed point $y = 1$. We therefore obtain the leading-order local normal form

$$\frac{dy}{d \ln a} = \frac{3}{p} y(1-y) + \mathcal{O}((1-y)^2). \quad (3.10)$$

Equation (3.10) is the one-dimensional normal form governing the approach to the density-controlled attractor [67]. The fixed points of the flow are

$$y = 0, \quad y = 1.$$

Linearizing the right-hand side of Eq. (3.10) about these points shows that $y = 0$ is unstable, while $y = 1$ is stable with eigenvalue given by Eq. (3.5). The effective index parameter of the logistic normal form is therefore

$$n = \frac{3}{p}. \quad (3.11)$$

Thus, the effective index parameter appearing in logistic parametrizations of IDE activation is not arbitrary, but determined by the local restoring order p of the scalar potential.

We stress that Eq. (3.10) is a local statement valid in the vicinity of the late-time fixed point. Far from the late-time fixed point, higher-order nonlinear terms and possible deviations from strict adiabatic tracking modify the global trajectory (see [68] for a detailed study). The logistic parametrization employed in phenomenological analyses should therefore be understood as a normal-form approximation capturing the universal asymptotic behavior of density-driven dark sector rather than an exact global solution.

3.3 Polynomial realization and explicit attractor exponents

We now consider explicitly that the \mathbb{Z}_2 -symmetric polynomial family satisfies the general attractor structure derived in Secs. 3.1 and 3.2. Consider the potential

$$V(\phi) = \frac{\lambda}{2m} (\phi^2 - v^2)^m, \quad m \geq 2, \quad (3.12)$$

which is equivalent to Eq. (2.13) after expanding around the VEV v in the absence of matter, with $\lambda > 0$. The quartic Mexican-hat potential corresponds to $m = 2$, while larger values of m describe progressively flatter minima generated by higher-dimensional operators in an EFT description [25, 69].

Differentiating Eq. (3.12) gives

$$V'(\phi) = \lambda \phi (\phi^2 - v^2)^{m-1}.$$

Let $\phi = v + \delta$, and $|\delta| \ll v$. Then

$$\phi^2 - v^2 = (v + \delta)^2 - v^2 = 2v\delta + \delta^2.$$

Expanding to leading order in $(\delta/v \ll 1)$, we obtain,

$$\phi^2 - v^2 = 2v\delta + \mathcal{O}(\delta^2), \quad \phi = v + \mathcal{O}(\delta),$$

which we substitute into $V'(\phi)$ and obtain

$$V'(\phi) = \lambda(v + \delta)(2v\delta)^{m-1} + \mathcal{O}(\delta^m) \quad (3.13)$$

$$= \lambda v(2v)^{m-1} \delta^{m-1} + \mathcal{O}(\delta^m). \quad (3.14)$$

Thus, the first non-vanishing term in the expansion of $V'(\phi)$ at the minimum is of order $p = m - 1$, in agreement with the general definition introduced in Eq. (3.1). The coefficient $\kappa_{m-1} = \lambda v(2v)^{m-1}$ is nonzero for $\lambda > 0$ and $v \neq 0$.

Substituting $p = m - 1$ into Eq. (3.5) gives $\lambda_p = -3/m - 1$. Accordingly, the displacement from the minimum obeys

$$\delta(a) \propto a^{-\frac{3}{m-1}}, \quad (3.15)$$

the index parameter of the logistic normal form (3.11) takes the form,

$$n = \frac{3}{m-1}. \quad (3.16)$$

consistent with the identification of the logistic index parameter in Eq. (3.11).

For the quartic case $m = 2$, one has $p = 1$, and therefore the attractor eigenvalue is $\lambda_p = -3$, corresponding to the canonical index $n = 3$. This reproduces the familiar exponential relaxation of a scalar field with finite curvature at the minimum. For $m > 2$, the restoring force is nonlinear, and the approach to the attractor becomes progressively slower as m increases.

The second derivative of the potential (3.12) is

$$V''(\phi) = \lambda(\phi^2 - v^2)^{m-1} + 2\lambda(m-1)\phi^2(\phi^2 - v^2)^{m-2}.$$

Evaluating at $\phi = v$ gives

$$V''(v) = \begin{cases} 2\lambda v^2, & m = 2, \\ 0, & m > 2, \end{cases}$$

indicating that the higher-order flatness of the minimum occurs in the absence of matter.

Thus, the vacuum curvature $V''(v)$ vanishes at tree level for $m > 2$, confirming that such minima are flat in the strict vacuum limit. Radiative corrections may lift the flatness of the minimum for ($m > 2$), although such effects can be suppressed within an EFT below the cutoff scale [9].

Since near the minimum $V'' \sim \delta^{m-2}$, along the cosmological tracking solution, the field is displaced by $\delta(a) \neq 0$. Thus, expanding $V''(\phi)$ near $\phi = v$ yields the leading scaling

$$V''(\phi_{\text{ad}}) \propto \lambda v^{2m-2} \left(\frac{\delta}{v} \right)^{m-2}. \quad (3.17)$$

Using Eq. (3.15), the effective mass along the trajectory scales as

$$m_{\text{eff}}^2(a) \sim \lambda v^{2m-2} a^{-\frac{3(m-2)}{m-1}}. \quad (3.18)$$

The prefactor λv^{2m-2} carries mass dimension two, ensuring dimensional consistency.

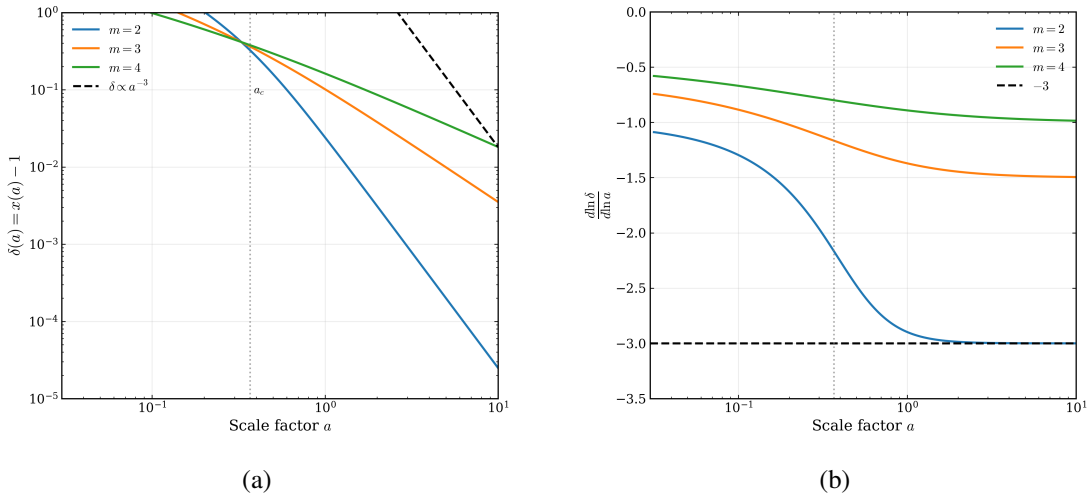


Figure 2: Late-time attractor dynamics for the polynomial potentials (3.12). Left: Displacement from the broken minimum, $\delta(a) = x(a) - 1$, for $m = 2, 3, 4$. At late times the solutions converge to the universal power-law scaling $\delta \propto a^{-3/(m-1)}$, in agreement with Eq. (3.15). Right: Instantaneous scaling exponent $d \ln \delta / d \ln a$ for the same models. The curves asymptote to the constant eigenvalues $-3, -3/2$, and -1 , confirming that the broken minimum is a hyperbolic fixed point with eigenvalue $\lambda_p = -3/(m-1)$.

We emphasize that (2.7) must be satisfied during the observationally relevant epoch. Since m_{eff}^2 decreases toward late times for $m > 2$, the most restrictive condition occurs near the transition epoch where δ is small but finite. When the microscopic scale satisfies $\lambda v^{2m-2} \gg H_0^2$, the hierarchy remains valid throughout the transition and late-time regime. However, consistency with the controlled perturbative regime requires that the induced energy exchange remain bounded by the condition $\max_a |\mathcal{E}(a)| < \epsilon_*$. For sufficiently small microscopic coupling and/or sufficiently large m_{eff}^2 , both conditions can be simultaneously satisfied. The polynomial family (3.12) therefore provides an explicit and internally consistent realization of the general attractor structure. The late-time exponent is determined solely by the local flatness of the symmetry-breaking minimum, with the quartic potential giving the maximally curved case and higher-order operators yielding systematically broadened density-driven crossovers.

3.4 Scope beyond polynomial potentials

Sections 3.1–3.3 showed that, for analytic symmetry-breaking potentials, the late-time approach to the density-controlled attractor is governed by the eigenvalue $\lambda_p = -3/p$, where p is the order of the first non-vanishing derivative of $V'(\phi)$ at the minimum. Within the class of analytic one-dimensional reductions considered here, this scaling is characteristic of systems near critical points [70–72]. We now clarify the general conditions under which this result holds beyond the polynomial class.

Consider a scalar potential (assuming $V'(\phi)$ is analytic at $\phi = v$) with local expansion

$$V'(\phi) = \kappa_p (\phi - v)^p + \mathcal{O}((\phi - v)^{p+1}), \quad (3.19)$$

Table 1: Representative symmetry-breaking potentials and their late-time attractor properties in the adiabatic regime. The attractor exponent depends only on the local order p of the first non-vanishing derivative of $V'(\phi)$ at the minimum, independent of the global form of the potential.

Potential type	Representative form	p	$\lambda_p = -3/p$	$n = 3/p$	Comments
Quartic (Mexican hat) [38, 76]	$\frac{\lambda}{4}(\phi^2 - v^2)^2$	1	-3	3	Non-degenerate minimum with $V''(v) = 2\lambda v^2$.
Higher-order polynomial ($m > 2$)	$\frac{\lambda}{2m}(\phi^2 - v^2)^m$	$m - 1$	$-\frac{3}{m-1}$	$\frac{3}{m-1}$	Flat minimum at tree level ($V''(v) = 0$); restoring force from higher-order operator.
Coleman-Weinberg (see [77])	$\frac{\lambda}{4}\phi^4\left(\ln\frac{\phi^2}{v^2} - \frac{1}{2}\right)$	1	-3	3	Radiative symmetry breaking; locally quadratic near the minimum.
Axion-like (see [78, 79])	$\Lambda^4[1 - \cos(\phi/f)]$	1	-3	3	Periodic potential; locally quadratic with $V''(v) = \Lambda^4/f^2$.

where $\kappa_p \neq 0$ and $p \geq 1$. Substituting this form into the density-controlled balance condition (2.10) yields

$$\delta(a) \equiv \phi_{\text{ad}}(a) - v \propto \rho_{\text{DM}}(a)^{1/p},$$

up to a constant prefactor determined by κ_p and β_c . In the controlled perturbative regime where $\rho_{\text{DM}} \propto a^{-3}$, the displacement scales as

$$\delta(a) \propto a^{-\frac{3}{p}}, \quad (3.20)$$

recovering the eigenvalue λ_p of Eq. (3.5). The late-time exponent therefore depends only on the local analytic structure of the potential near the minimum, provided the tracking hierarchy remains valid.

However, this result holds only under well-defined conditions. Specifically, it requires: (i) the existence of a smooth and isolated minimum at $\phi = v$, (ii) a valid local Taylor expansion of $V'(\phi)$ about that minimum, and (iii) the validity of the controlled tracking regime, and (iv) the absence of additional time-dependent sources or couplings that modify the dilution law. If these assumptions are violated, for instance, in the presence of non-analytic cusps [73, 74], multiple competing minima [75], or significant departures from the perturbative regime, the late-time scaling may be modified.

Table 1 summarizes representative realizations and their corresponding attractor classes. Radiatively generated symmetry-breaking potentials such as the Coleman-Weinberg form, as well as periodic axion-like models expanded about a minimum, possess non-degenerate analytic minima ($p = 1$) and therefore yield the canonical eigenvalue $\lambda_p = -3$ and index parameter $n = 3$. In contrast, higher-order polynomial potentials with $m > 2$ exhibit flat minima at tree level ($p = m - 1$) and consequently produce softened attractor exponents $\lambda_p = -3/(m - 1)$.

The logistic normal form (3.10) should therefore be interpreted as the local description of density-controlled symmetry breaking in the dark sector. Allowing the phenomenological index parameter n to vary corresponds to scanning over different restoring operators in the underlying scalar theory, while fixing $n = 3$ selects the class of non-degenerate analytic minima. Thus, n acquires a microscopic interpretation as the inverse of the local restoring order p .

4 Emergent Effective Coupling and Logistic Activation

The preceding section showed that the late-time approach to the symmetry-breaking minimum can be described by a logistic normal-form approximation, with the index parameter $n = 3/p$ determined by the local restoring order p of the scalar potential. We now demonstrate how this attractor dynamics translates into a specific redshift-dependent coupling in the dark sector.

Recall that along the density-controlled tracking trajectory, the field evolves according to the autonomous flow equation (2.21). In the vicinity of the broken minimum, the displacement $\delta(a) \equiv \phi_{\text{ad}}(a) - v$ obeys the linearized flow (3.4), which we rewrite using the identification $n = 3/p$ as

$$\frac{d\delta}{d\ln a} = -n\delta + \mathcal{O}(\delta^2). \quad (4.1)$$

To capture the leading nonlinear behavior over a finite redshift interval, it is convenient to introduce the inverse order parameter

$$y(a) \equiv \frac{v}{\phi_{\text{ad}}(a)} = \frac{1}{x(a)}, \quad (4.2)$$

which approaches unity as the field relaxes toward the symmetry-breaking minimum.

Expanding the full autonomous flow around $y = 1$ and retaining the leading nonlinear term yields the normal form already derived in Eq. (3.10):

$$\frac{dy}{d\ln a} = ny(1-y) + \mathcal{O}((1-y)^2). \quad (4.3)$$

At leading order, Eq. (4.3) is approximated by the logistic solution

$$y(a) = \frac{(a/a_c)^n}{1 + (a/a_c)^n}, \quad (4.4)$$

where the integration constant is expressed in terms of the critical scale factor a_c defined by $y(a_c) = 1/2$. This effectively marks the epoch at which the density-induced deformation parameter $\xi(a)$ defined in Eq. (2.18) becomes of order unity, signaling the transition from the density-dominated regime to the vacuum-dominated regime. To translate this attractor dynamics into the interaction sector, we now specify the effective coupling used in the cosmological analysis. In the scalar–tensor framework of Sec. 2, the interaction arises from a conformal coupling to DM, so that the effective coupling is evaluated along the tracking solution $\phi_{\text{ad}}(a)$.

In the perturbative regime of interest, we adopt a minimal effective description in which the coupling inherits the activation profile of the symmetry-breaking order parameter. Since the scalar displacement governs the interaction strength along the attractor solution, we adopt

$$\beta_{\text{eff}}(a) = \beta_0 y(a), \quad (4.5)$$

where $y(a) = v/\phi_{\text{ad}}(a)$ is given by Eq. (4.4) and β_0 denotes the asymptotic coupling strength at late times. Substituting the logistic solution (4.4) into the effective mapping (4.5) yields the activation profile

$$\beta(a) = \beta_0 \frac{a^n}{a^n + a_c^n}, \quad (4.6)$$

where $\beta_0 \equiv \beta(v)$ sets the asymptotic coupling strength in the vacuum (see [38] for details).

Within this effective description, the parameters in Eq. (4.6) have the following interpretation. The index $n = 3/p$ is determined by the local restoring order of the symmetry-breaking potential, with $n = 3$ corresponding to a non-degenerate analytic minimum (e.g., the quartic Mexican-hat potential), while smaller values correspond to progressively flatter minima arising from higher-order operators. The activation scale a_c is determined by the condition $\xi(a_c) = \mathcal{O}(1)$ in Eq. (2.18) and represents the epoch at which the density-induced deformation becomes comparable to the intrinsic restoring scale of the scalar potential.

Equation (4.6) therefore defines the leading-order activation profile implied by the attractor dynamics. It describes a dark sector interaction that remains suppressed at early times and activates smoothly at late times, with a shape controlled by the curvature of the underlying scalar potential. The parameters n and a_c are thus not arbitrary phenomenological inputs but encode the microscopic structure of the scalar sector.

In the following section, we implement the parametrization of Eq. (4.6) in a Boltzmann solver and confront it with cosmological observations, with the understanding that n encodes the local restoring structure of the underlying scalar potential.

5 Methodology and Numerical Implementation

This section describes the numerical implementation of the IDE model and the statistical framework used to confront the theory with cosmological observations. We first specify the hierarchy of cosmological models and parameterizations used in the analysis. We then outline the perturbative consistency conditions, the implementation of the interaction in the Boltzmann solver CLASS, and the datasets and statistical procedures used for parameter inference.

5.1 Model hierarchy and parameterization

We consider three nested realizations of the IDE scenario discussed in the previous sections. The models share identical likelihood construction and prior assumptions and differ only in the structure of the interaction sector. While the microphysical derivation predicts discrete values for $n = 3/p$, we treat n as a continuous parameter in our statistical analysis. This allows the data to test whether the preferred curvature class lies near one of the discrete microphysical values. The posterior constraints can then be interpreted in terms of the underlying scalar potential through the relationship $p = 3/n$.

(i) Six-parameter IDE model. The most general realization is defined by

$$\Theta_{6p} = (\Omega_m, h, \sigma_8, \beta_0, a_c, n). \quad (5.1)$$

The priors are

$$\begin{aligned} \Omega_m &\in (0.2, 0.4), & h &\in (0.55, 0.85), & \sigma_8 &\in (0.6, 1.0), \\ \beta_0 &\in (-0.3, 0.3), & a_c &\in (0.1, 1.0), & n &\in (0.5, 5.0), \end{aligned}$$

with the physical constraint $\Omega_m h^2 > 0.02237$. In this realization the restoring order of the symmetry-breaking minimum is treated as a free parameter through the relation $n = 3/p$.

(ii) Fixed-index IDE model. To isolate the amplitude and activation scale of the interaction, we also consider a restricted realization in which the index parameter is fixed to its canonical value $n = 3$, corresponding to a non-degenerate analytic minimum ($p = 1$). The sampled parameter vector becomes

$$\Theta_{5p} = (\Omega_m, h, \sigma_8, \beta_0, a_c). \quad (5.2)$$

(iii) Λ CDM limit. In the limit $\beta_0 \rightarrow 0$ the effective coupling vanishes and the model reduces to standard Λ CDM,

$$\Theta_{\Lambda\text{CDM}} = (\Omega_m, h, \sigma_8). \quad (5.3)$$

The baryon density Ω_b , scalar spectral index n_s , and optical depth τ are fixed to their *Planck* 2018 best-fit values [5]. The parameter σ_8 is internally mapped to the primordial amplitude A_s within the Boltzmann solver CLASS [80].

5.2 Controlled perturbative regime and post-chain filtering

All theoretical developments in Secs. 2–4 assume the controlled perturbative regime defined in Sec. 2.3, where the energy exchange between DM and the scalar field remains small compared to the standard Hubble dilution term. This regime is quantified by

$$\max_a |\varepsilon(a)| < \varepsilon_*, \quad \varepsilon_* = 10^{-2}. \quad (5.4)$$

For each posterior sample obtained from the MCMC analysis, the quantity $\varepsilon(a)$ is evaluated along the adiabatic tracking solution $\phi_{\text{ad}}(a)$ using the relation derived in Sec. 2.3 (see Appendix B for the reduced continuity equation). The maximum value of $|\varepsilon(a)|$ is computed over the redshift interval $0 \leq z \leq 2$, corresponding to the range probed by the RSD and SN data. Samples satisfying Eq. (5.4) are retained, while those violating the bound are discarded in a post-processing step. The perturbative criterion is therefore applied after chain convergence, leaving the likelihood function unchanged while isolating the region of parameter space where the perturbative background treatment remains valid.

Table 2 reports the fraction of posterior samples satisfying the perturbative bound for each dataset combination. As expected, the Λ CDM limit satisfies the bound identically. For the full six-parameter IDE model, roughly half of the posterior volume lies within the controlled regime. Fixing the index parameter to $n = 3$ reduces the surviving fraction, reflecting the reduced flexibility of the interaction sector. Importantly, the filtering procedure does not alter the likelihood evaluation itself but only identifies the subset of statistically allowed cosmologies for which the perturbative assumptions remain valid. All reported parameter constraints, therefore, refer to the posterior subset that satisfies the theoretical consistency condition.

5.3 Linear perturbation implementation in CLASS

The IDE model was implemented in a modified version of the Boltzmann solver CLASS [80]. Within the controlled perturbative regime defined in Sec. 5.2, the energy exchange between DM and the scalar field remains sufficiently small that the background expansion can be approximated by its Λ CDM form,

$$H^2(a) = H_0^2 [\Omega_m a^{-3} + (1 - \Omega_m)]. \quad (5.5)$$

Table 2: Fraction of posterior samples satisfying the perturbative consistency condition $\max_a |\varepsilon(a)| < 10^{-2}$ for each dataset combination and model realization.

Dataset	Model	Acceptance Fraction
RSD	Λ CDM	1.000
RSD	IDE (6p)	0.492
RSD	IDE ($n = 3$)	0.333
Planck+RSD	Λ CDM	1.000
Planck+RSD	IDE (6p)	0.486
Planck+RSD	IDE ($n = 3$)	0.290
Planck+RSD+SN	Λ CDM	1.000
Planck+RSD+SN	IDE (6p)	0.485
Planck+RSD+SN	IDE ($n = 3$)	0.220

Interaction effects are incorporated only at the level of linear perturbations. The scalar field is integrated into the perturbation system through the time-dependent effective coupling $\beta(a)$, which is derived in Section 4. This coupling is implemented as a covariant energy-momentum transfer aligned with the CDM four-velocity. Baryons, photons, and neutrinos evolve according to their standard Λ CDM equations.

The modified solver evolves the full Einstein-Boltzmann system to compute linear observables, including the matter power spectrum $P(k, z)$, the growth rate $f(z)$, and the CMB lensing potential $C_L^{\phi\phi}$. The linear perturbation analysis is valid on scales where perturbations remain linear, roughly ($k \lesssim 0.1 h \text{Mpc}^{-1}$ at $z = 0$), with the precise range depending on redshift. For the redshift-space distortion data used in this analysis [55], which primarily probe quasi-linear scales, the linear treatment remains adequate for the conservative k -cuts applied to the observational samples (typically $k_{\text{max}} \sim 0.1 h \text{Mpc}^{-1}$ at the effective redshift of each measurement). Nonlinear corrections to the matter power spectrum are not expected to significantly affect the conclusions, as the interaction primarily modifies the growth history on linear scales and the data are analyzed within the regime where linear theory is reliable.

Numerical consistency was verified by cross-checking the implementation in both Newtonian and synchronous gauges. In the limit where $\beta_0 \rightarrow 0$, the code reproduces the standard Λ CDM spectra with machine precision.

5.4 Data sets and statistical analysis

We confront the IDE scenario with a combination of late-time geometric and structure-growth observables. All theoretical predictions entering the likelihood evaluation are obtained from the modified CLASS solver described in Sec. 5.3. Only parameter samples satisfying the perturbative consistency condition of Sec. 5.2 are retained in the final analysis.

CMB lensing (Planck 2018). We use the *Planck* 2018 CMB lensing reconstruction [5], which measures the lensing potential power spectrum $C_L^{\phi\phi}$ over multipoles $8 \leq L \leq 400$. The likelihood

is computed as

$$\chi_{\text{Planck}}^2 = (\mathbf{C}^{\text{th}} - \mathbf{C}^{\text{obs}})^{\text{T}} \mathbf{Cov}^{-1} (\mathbf{C}^{\text{th}} - \mathbf{C}^{\text{obs}}). \quad (5.6)$$

Redshift-space distortions. Growth constraints are obtained from measurements of $f\sigma_8(z)$ [55]. The theoretical prediction is

$$f\sigma_8(z) = f(z) \sigma_8 \frac{D(z)}{D(0)}, \quad (5.7)$$

with likelihood

$$\chi_{\text{RSD}}^2 = \sum_i \frac{[f\sigma_8^{\text{th}}(z_i) - f\sigma_8^{\text{obs}}(z_i)]^2}{\sigma_i^2}. \quad (5.8)$$

Type Ia supernovae. When included, the Pantheon+SH0ES sample [81] constrains the luminosity distance through

$$\chi_{\text{SN}}^2 = (\boldsymbol{\mu}^{\text{th}} - \boldsymbol{\mu}^{\text{obs}})^{\text{T}} \mathbf{Cov}^{-1} (\boldsymbol{\mu}^{\text{th}} - \boldsymbol{\mu}^{\text{obs}}). \quad (5.9)$$

The combined likelihood is

$$\chi_{\text{tot}}^2 = \chi_{\text{Planck}}^2 + \chi_{\text{RSD}}^2 + \chi_{\text{SN}}^2. \quad (5.10)$$

Parameter inference is performed using the affine-invariant ensemble sampler `emcee` [82]. The posterior distribution is

$$\mathcal{P}(\Theta|\text{data}) \propto \exp\left[-\frac{1}{2}\chi_{\text{tot}}^2(\Theta)\right] \Pi(\Theta), \quad (5.11)$$

where $\Pi(\Theta)$ denotes the uniform priors specified in Sec. 5.1. Chains are evolved until convergence, and burn-in segments are discarded prior to posterior estimation.

6 Observational Constraints and Analysis

This section presents the observational constraints on the IDE scenario using the methodology described in Sec. 5. We first analyze the fully flexible six-parameter realization of the activation model and assess its statistical consistency with Λ CDM across progressively informative dataset combinations. We then examine the phenomenology of the growth sector and investigate how the posterior structure changes when the activation index is fixed, along with the implications for the dimensionality of the interaction history.

6.1 Flexible six-parameter IDE model: posterior structure and null detection

We first analyze the fully flexible six-parameter realization of the IDE scenario introduced in Sec. 5.1, in which the interaction follows the logistic activation derived in Sec. 4. Constraints are obtained using three progressively informative dataset combinations (RSD only, Planck+RSD, and Planck+RSD+SN), and the resulting posterior constraints and model-comparison diagnostics are summarized in Table 3.

Table 3: Marginalized constraints on the six-parameter IDE model. For each parameter we report the posterior median, the 68% and 95% credible intervals, and the marginal Kullback–Leibler (KL) divergence (in nats), which quantifies the information gain relative to the uniform priors adopted in Sec. 5.1.

Parameter	Median	68% C.L.	95% C.L.	KL (nats)
RSD only				
Ω_m	0.2996	[0.2313, 0.3667]	[0.2046, 0.3951]	0.005
h	0.7039	[0.5993, 0.8059]	[0.5575, 0.8440]	0.004
σ_8	0.8134	[0.6744, 0.9424]	[0.6118, 0.9910]	0.009
β_0	-0.0001	[-0.1346, 0.1325]	[-0.2646, 0.2641]	0.159
a_c	0.6338	[0.3319, 0.8925]	[0.1510, 0.9825]	0.041
n	1.6191	[0.8222, 3.3981]	[0.5505, 4.7220]	0.364
Planck + RSD				
Ω_m	0.3037	[0.2337, 0.3684]	[0.2052, 0.3956]	0.007
h	0.7024	[0.5978, 0.8051]	[0.5575, 0.8424]	0.005
σ_8	0.7918	[0.6539, 0.9382]	[0.6094, 0.9905]	0.007
β_0	-0.0012	[-0.1309, 0.1205]	[-0.2616, 0.2647]	0.177
a_c	0.6367	[0.3474, 0.8885]	[0.1620, 0.9789]	0.052
n	1.7086	[0.8243, 3.5038]	[0.5421, 4.7546]	0.323
Planck + RSD + SN				
Ω_m	0.3603	[0.3409, 0.3785]	[0.3234, 0.3938]	0.989
h	0.7059	[0.6002, 0.8015]	[0.5583, 0.8414]	0.009
σ_8	0.8076	[0.6694, 0.9397]	[0.6104, 0.9906]	0.006
β_0	0.0115	[-0.1209, 0.1518]	[-0.2588, 0.2741]	0.139
a_c	0.6269	[0.3449, 0.8946]	[0.1659, 0.9836]	0.049
n	1.6916	[0.8318, 3.4971]	[0.5472, 4.7616]	0.323

Across all dataset combinations, the background parameters (Ω_m, h) and the clustering amplitude σ_8 remain tightly constrained at levels comparable to Λ CDM. For the most constraining dataset combination (Planck+RSD+SN), we obtain $\Omega_m = 0.3603^{+0.0182}_{-0.0194}$, $h = 0.7059^{+0.0956}_{-0.1057}$, and $\sigma_8 = 0.8076^{+0.1321}_{-0.1382}$. The comparatively broad constraint on h reflects the absence of primary CMB anisotropy data in the likelihood. Posterior medians remain close to the maximum-likelihood values, and no parameter accumulates near prior boundaries, indicating a regular likelihood surface within the adopted parameter ranges. However, the interaction parameters remain weakly constrained. The coupling amplitude β_0 is statistically consistent with zero for all dataset combinations, with posterior intervals centered near $\beta_0 \approx 0$. The critical scale factor a_c and the index parameter n remain broadly distributed across their prior ranges. The marginal KL divergences reported in Table 3 quantify this hierarchy of information gain. This shows that supernova data primarily tighten the constraint on Ω_m , while the interaction parameters acquire

Table 4: Statistical comparison between Λ CDM and IDE (6p). We report the minimum χ^2 , the Akaike and Bayesian information criteria differences, and the Laplace-approximated Bayesian evidence difference $\Delta \log Z = \log Z_{\text{IDE}} - \log Z_{\Lambda\text{CDM}}$. Positive values favor IDE, while negative values favor Λ CDM.

Dataset	Model	χ^2_{min}	ΔAIC	ΔBIC	$\Delta \log Z$
RSD	Λ CDM	1173.29	0	0	0
	IDE (6p)	1173.29	+6.00	+7.19	-1.396
Planck+RSD	Λ CDM	2622.07	0	0	0
	IDE (6p)	2622.07	+6.00	+9.66	-1.404
Planck+RSD+SN	Λ CDM	4431.02	0	0	0
	IDE (6p)	4431.02	+6.00	+22.36	-1.41

only modest information relative to their prior volumes. This behavior suggests that current observations constrain the overall amplitude of late-time growth and geometry but do not significantly specify the detailed redshift structure of the activation history.

The qualitative variation of IDE posteriors across dataset combinations reflects a rotation of degeneracy directions between growth-sector and geometric parameters. Within the controlled perturbative regime, the homogeneous expansion is fixed to its Λ CDM form, so interaction effects enter only through the linear growth sector. RSD measurements therefore constrain combinations of Ω_m and the effective friction modification induced by $\beta(a)$, generating a degeneracy direction in which shifts in Ω_m can be partially compensated by changes in β_0 and, to a lesser extent, by the activation parameters (a_c, n) . When supernova data are added, the geometry tightly constrains Ω_m , collapsing this degeneracy direction and reshaping the projected posterior for the interaction parameters. The resulting dataset dependence does not indicate instability of the interacting sector, but rather reflects the complementary sensitivity of growth and geometric observables in parameter space.

A direct statistical comparison with Λ CDM is presented in Table 4. For all dataset combinations, the minimum χ^2 values of the IDE (6p) model and Λ CDM are statistically indistinguishable, yielding $\Delta\chi^2 \simeq 0$ within numerical accuracy. Information criteria penalize the additional three IDE parameters as expected from the model dimensionality, with $\Delta\text{AIC} \simeq 6$ and larger ΔBIC values for the most data-rich combination. The Bayesian evidence difference remains small ($\Delta \log Z \approx -1.4$) and corresponds at most to weak evidence in favor of Λ CDM. Taken together, these diagnostics indicate that present observations neither require nor statistically favor the interacting scenario relative to Λ CDM. At the same time, the interaction sector retains substantial degeneracy freedom, showing the limited sensitivity of current data to the detailed functional form of the activation history. In particular, the posterior does not exhibit compression toward prior boundaries in any parameter direction, distinguishing the flexible realization from the restricted fixed-index case discussed in Sec. 6.3.

6.2 Growth-sector phenomenology under flexible activation

We first examine the phenomenology of the flexible six-parameter (6p) realization, in which the activation index n is allowed to vary freely. Throughout this analysis, the homogeneous expansion history is fixed to its Λ CDM form within the controlled perturbative regime defined in Sec. 5.2. Consequently, all observable effects of the interacting sector arise exclusively through modifications of linear perturbations. Geometric observables therefore remain unchanged by construction, and any deviation from Λ CDM must manifest in the growth sector.

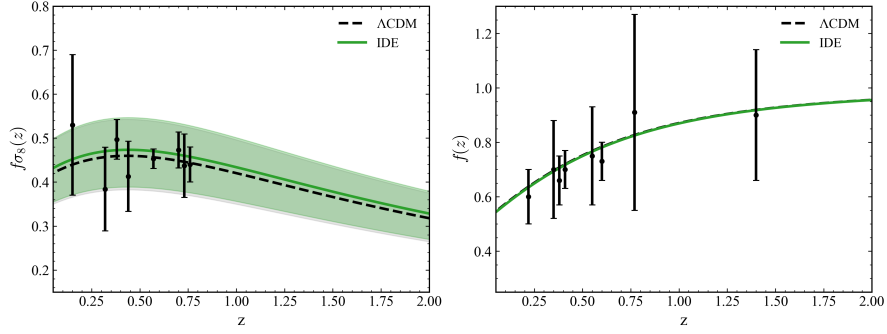
To visualize the observable consequences of the interaction, we examine the posterior predictions for the linear growth observables. Figure 3 shows the posterior predictions for the linear growth rate $f(z)$ and the observable $f\sigma_8(z)$ for the three dataset combinations considered. Across the redshift range $0 < z < 2$, the IDE (6p) posterior envelopes remain statistically consistent with Λ CDM within the 68% credible regions. The largest deviations occur at low redshift, where the logistic activation becomes dynamically relevant, but remain confined to the percent level. Quantitatively, the fractional shift in $f\sigma_8$ at $z = 0$ is small for all dataset combinations: a 0.53% suppression for RSD-only, a 1.44% enhancement for Planck+RSD, and a 0.11% enhancement for Planck+RSD+SN. The sign of the shift follows the posterior preference for the coupling parameter β_0 , which remains tightly constrained around zero (Table 3). Within the perturbative regime, modifications of the growth equation scale with the effective coupling and become relevant only after the activation epoch ($a \gtrsim a_c$). Because the activation is both redshift-localized and of small amplitude, the integrated correction to the growth history remains suppressed. Current data, therefore, limit posterior-allowed growth-sector deviations to the percent level, without requiring the interaction amplitude to vanish.

The impact on the derived clustering parameter $S_8 \equiv \sigma_8 \sqrt{\Omega_m/0.3}$ is correspondingly small. Figure 4 shows the posterior correlation between S_8 and the interaction amplitude β_0 after perturbative filtering. The Pearson correlation coefficients satisfy $|\rho| \lesssim 0.08$ for all dataset combinations, indicating that the interaction strength and clustering amplitude span nearly orthogonal directions in parameter space. Although a mild trend is visible for the most constraining dataset combination, its magnitude remains small compared to the intrinsic posterior width of S_8 . The flexible activation, therefore, does not generate a statistically significant shift in the inferred clustering normalization relative to Λ CDM. This behavior is consistent with the model-comparison results of Sec. 6.1, which show no statistical preference for IDE relative to Λ CDM. Current observations, therefore, constrain any density-activated interaction to remain perturbative, with only small effects on late-time structure formation.

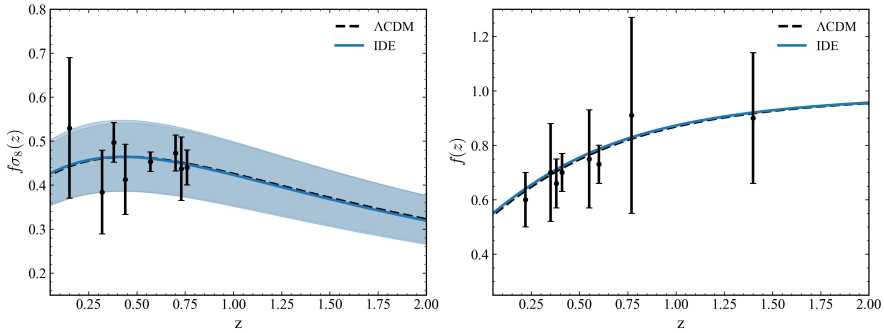
In summary, when the activation profile retains full functional freedom (i.e., when n is allowed to vary), the interacting scenario remains observationally viable and statistically indistinguishable from Λ CDM at current observational precision. Deviations arise solely in the growth sector, are localized at late times, and are limited in magnitude by the posterior constraint on β_0 . In the next subsection, we examine how these conclusions change when the activation index is fixed, thereby removing one degree of freedom from the interaction history.

6.3 Fixed-index realization and degeneracy compression

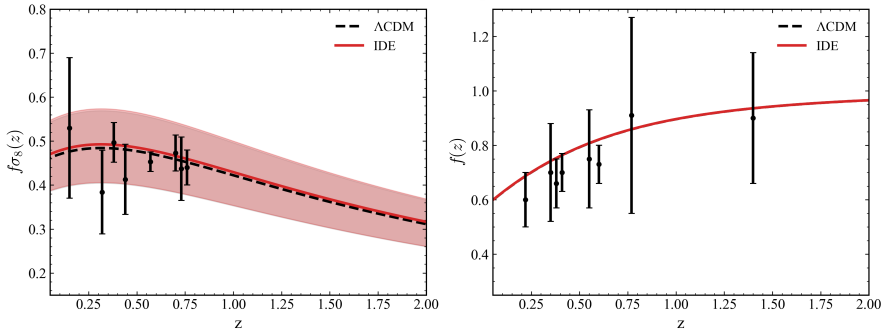
To assess the structural role of the activation profile, we consider a restricted realization in which the index parameter is fixed to the canonical value $n = 3$, corresponding to a non-degenerate



(a) RSD only



(b) Planck + RSD



(c) Planck + RSD + SN

Figure 3: Redshift evolution of the linear growth observables $f\sigma_8(z)$ and $f(z)$ in the IDE (6p) model for three dataset combinations: (a) RSD only, (b) Planck+RSD, and (c) Planck+RSD+SN. Solid curves denote posterior mean predictions, with shaded bands showing 68% credible regions. Across all datasets, deviations from Λ CDM remain at the percent level at $z=0$ and within current observational uncertainties.

analytic minimum of the underlying scalar potential. This reduces the interaction sector by one functional degree of freedom while keeping all priors, datasets, and perturbative consistency

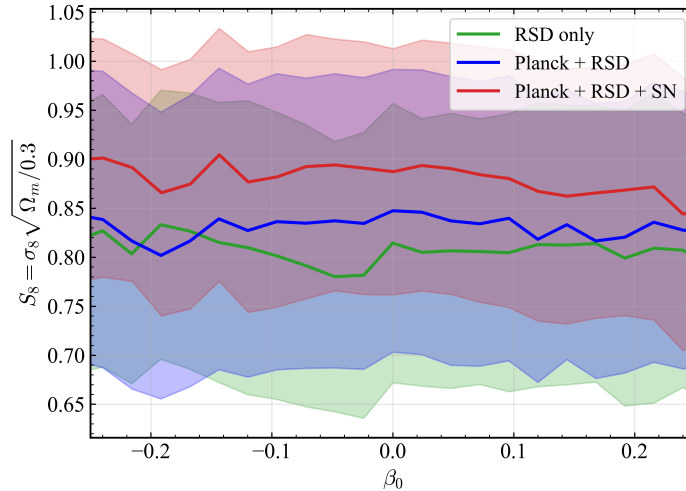


Figure 4: Posterior-averaged dependence of $S_8 = \sigma_8 \sqrt{\Omega_m/0.3}$ on the interaction amplitude β_0 in the IDE (6p) model. The weak slope and small correlation coefficient indicate near-orthogonality between the interaction strength and late-time clustering normalization, implying minimal degeneracy in the combined Planck+RSD+SN fit.

conditions identical to those of the six-parameter (6p) analysis.

The marginalized constraints for the fixed-index model are summarized in Table 5. For the RSD-only and Planck+RSD combinations, the posterior distributions of $(\Omega_m, h, \sigma_8, \beta_0, a_c)$ remain statistically comparable to the flexible 6p case. Credible intervals and best-fit values are similar, and the minimum χ^2 values are indistinguishable within sampling precision. These datasets primarily constrain perturbation growth and clustering amplitude and therefore do not strongly probe the detailed redshift structure of the activation profile. Within this restricted information set, fixing n does not significantly modify the likelihood geometry.

The situation changes once Type Ia supernova data are included. Supernova distances tightly constrain the late-time expansion history and thereby couple geometric and growth information. Although the homogeneous background is fixed to Λ CDM by construction, the interaction modifies perturbations in a redshift-dependent manner. When n is allowed to vary, the activation index provides additional freedom to redistribute perturbative effects across redshift while remaining consistent with the supernova Hubble diagram. Fixing n removes this compensating direction and therefore alters the degeneracy structure of the parameter space.

The fixed-index realization remains statistically acceptable with respect to the supernova Hubble diagram, although it performs worse than the flexible n case. Using the Planck+RSD+SN best-fit parameters, we obtain

$$\chi_{\text{SN}}^2 = 1808.96 \quad (\text{IDE 6p}), \quad \chi_{\text{SN}}^2 \simeq 1901 \quad (\text{IDE } n = 3),$$

corresponding to $\chi_{\text{SN}}^2/\text{dof} \simeq 1.06$ and 1.12, respectively. The increase $\Delta\chi_{\text{SN}}^2 \simeq 92$ is distributed over $N_{\text{SN}} = 1701$ supernovae and therefore corresponds to a small change in the average residual

Table 5: Marginalized constraints for the IDE model with fixed $n = 3$. For each parameter we report the posterior median, the 68% and 95% credible intervals, and the marginal Kullback-Leibler (KL) divergence (in nats) relative to the same uniform priors as in Tab. 3.

Parameter	Median	68% C.L.	95% C.L.	KL (nats)
RSD only ($n = 3$)				
Ω_m	0.3068	[0.2332, 0.3713]	[0.2047, 0.3964]	0.007
h	0.7101	[0.6063, 0.8045]	[0.5606, 0.8419]	0.012
σ_8	0.7931	[0.6628, 0.9296]	[0.6098, 0.9885]	0.008
β_0	0.0011	[-0.0803, 0.0810]	[-0.1424, 0.1479]	0.652
a_c	0.7217	[0.4115, 0.9247]	[0.1996, 0.9863]	0.128
Planck + RSD ($n = 3$)				
Ω_m	0.3019	[0.2345, 0.3684]	[0.2056, 0.3945]	0.008
h	0.7148	[0.6082, 0.8063]	[0.5601, 0.8423]	0.014
σ_8	0.7944	[0.6593, 0.9342]	[0.6082, 0.9900]	0.005
β_0	0.0000	[-0.0839, 0.0835]	[-0.1479, 0.1437]	0.638
a_c	0.7183	[0.4199, 0.9242]	[0.1927, 0.9879]	0.128
Planck + RSD + SN ($n = 3$)				
Ω_m	0.2017	[0.2000, 0.2254]	[0.2000, 0.2468]	1.903
h	0.5813	[0.5500, 0.6982]	[0.5500, 0.7063]	0.825
σ_8	0.6040	[0.6000, 0.6203]	[0.6000, 0.7730]	2.251
β_0	-0.0090	[-0.0603, 0.0539]	[-0.1284, 0.1199]	0.907
a_c	0.5306	[0.2465, 0.9033]	[0.1952, 0.9972]	0.067

per data point. Both realizations remain statistically acceptable descriptions of the supernova Hubble diagram, although the flexible 6p model yields the smaller χ^2 . The supernova residuals relative to the best-fit luminosity distance predictions are shown in Fig. 5. While the fixed-index model exhibits a somewhat larger dispersion of residuals at intermediate redshift, no systematic drift or runaway behaviour is observed. The difference relative to the flexible 6p case is therefore quantitative rather than qualitative.

The principal effect of fixing n appears in the structure of the posterior manifold rather than in the overall goodness-of-fit. For the Planck+RSD+SN combination, the marginalized distributions of Ω_m , h , and σ_8 contract substantially and accumulate near the lower prior boundaries, as shown in Table 6. This boundary accumulation indicates that fixing n exposes a prior-truncated degeneracy direction; the contraction is therefore not purely data-driven. For example, the posterior width of σ_8 decreases by more than a factor of three relative to the 6p realization, and a large fraction of samples lie within 5% of the lower prior limits for Ω_m and σ_8 . The likelihood peak remains comparable in height to the 6p realization, and the contraction is not accompanied by any improvement in χ^2 , indicating that the reduced parameter volume reflects loss of degeneracy freedom rather than a statistical preference of the data.

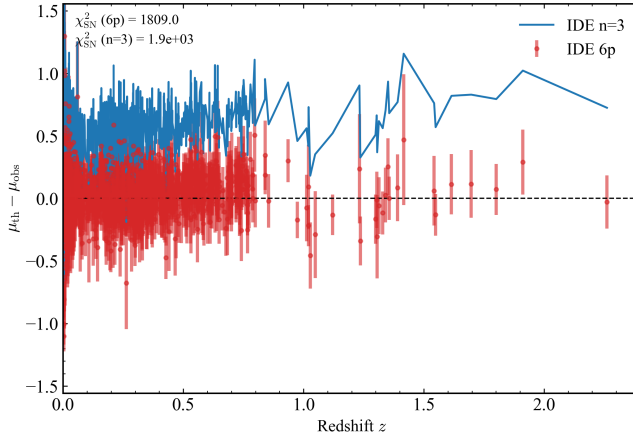


Figure 5: Supernova Hubble-diagram residuals $\mu_{\text{th}} - \mu_{\text{obs}}$ for the Planck+RSD+SN best-fit cosmologies in the flexible IDE (6p) and fixed-index ($n = 3$) realizations. The 6p model yields $\chi_{\text{SN}}^2 = 1809$ for $N_{\text{SN}} = 1701$ ($\chi^2/\text{dof} \simeq 1.06$), statistically comparable to ΛCDM . The fixed-index realization produces a slightly larger χ_{SN}^2 , corresponding to a small change in the average supernova residual.

Table 6: Posterior geometry diagnostics for the IDE model using the Planck + RSD + SN dataset combination. We report the marginalized posterior median, standard deviation, the distance of the median from the lower prior boundary in units of the posterior standard deviation, the width ratio relative to the full six-parameter model, and the fraction of samples lying within 5% of the lower and upper prior boundaries. These diagnostics illustrate the change in posterior structure when the activation index is fixed ($n = 3$), noting that posterior widths may be affected by truncation near prior boundaries.

Parameter	Model	Median	Std	(Median - Lower)/ σ	Width Ratio	% near lower / upper
Ω_m	IDE 6p	0.35997	0.01908	8.38	1.00	0.00% / 4.36%
	IDE $n = 3$	0.20029	0.01413	0.02	1.35	87.26% / 0.01%
h	IDE 6p	0.70528	0.08528	1.82	1.00	4.52% / 4.70%
	IDE $n = 3$	0.55036	0.05815	0.01	1.47	70.74% / 0.00%
σ_8	IDE 6p	0.80763	0.11473	1.81	1.00	4.70% / 5.30%
	IDE $n = 3$	0.60510	0.03417	0.15	3.36	91.97% / 0.05%

The change in degeneracy geometry is further illustrated in Fig. 6, which shows the Pearson correlation coefficients between S_8 and the interaction parameters. In the flexible 6p model, correlations remain mild and statistically consistent with zero across dataset combinations, indicating the presence of an extended, approximately flat direction in parameter space. When n is fixed, structured correlations emerge under the Planck+RSD+SN constraint, most notably between S_8 and a_c . This behaviour reflects the reduced freedom to redistribute perturbative effects across redshift once the activation index is fixed. The posterior manifold, therefore, becomes more anisotropic, and the previously weakly curved direction associated with variations in n acquires significant curvature.

The fixed-index realization, therefore, remains observationally viable but structurally more rigid. Current data do not require a nonzero interaction amplitude, but they exhibit limited

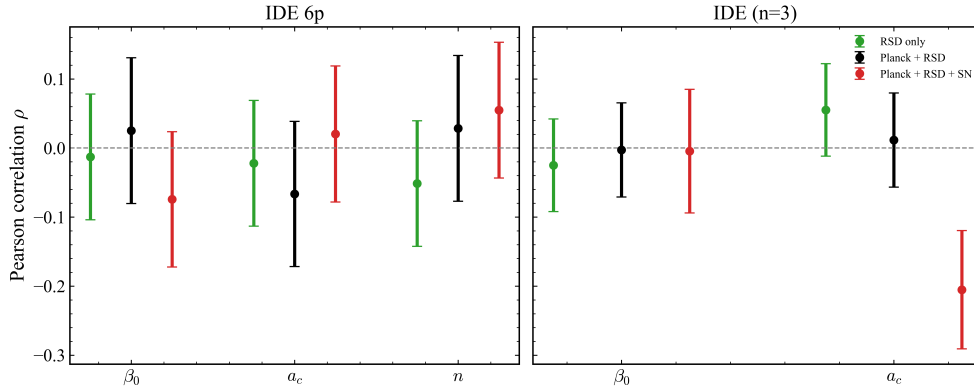


Figure 6: Points show the Pearson correlation coefficient $\rho(S_8, \theta)$ for each parameter θ , with analytic 1σ uncertainties derived from the Fisher z -transform using the effective sample size. Green, black, and red correspond to RSD only, Planck+RSD, and Planck+RSD+SN datasets, respectively. In the flexible 6p realization, correlations remain mild and statistically consistent with zero, indicating an extended degeneracy direction in parameter space. When the activation index is fixed ($n = 3$, right panel), more structured correlations emerge—most notably between S_8 and a_c for the Planck+RSD+SN combination, indicating the reduced freedom to redistribute perturbative effects across redshift.

sensitivity to the dimensionality of the redshift-dependent activation history. Allowing n to vary preserves an interior, weakly curved likelihood region consistent with both geometric and growth observables. Imposing $n = 3$ reduces this interior volume without improving the goodness-of-fit, demonstrating that functional flexibility in the activation profile plays a nontrivial role in preserving degeneracy structure under combined geometric and growth constraints.

6.4 Structural implications of observational constraints

Previous sections established a consistent empirical pattern: current cosmological data do not require a nonzero interaction amplitude, and the fully flexible six-parameter (6p) realization remains statistically indistinguishable from Λ CDM within present precision. When the activation index n is allowed to vary, the posterior occupies an extended interior region of parameter space. The interaction amplitude β_0 is constrained to remain perturbatively small, and deviations in growth observables are limited to the percent level at low redshift. At the same time, the activation parameters (a_c, n) retain substantial degeneracy freedom, reflecting the limited sensitivity of present data to the detailed temporal structure of the coupling.

Within the scalar-tensor realization introduced earlier, the activation index is related to the curvature structure of the scalar potential through the relation $n = 3/p$, where p denotes the order of the first nonvanishing derivative of $V'(\phi)$ at the symmetry-breaking minimum. Treating n as a continuous parameter in the statistical analysis, therefore, allows the observational constraints to be mapped onto classes of scalar potentials characterized by different restoring orders. The posterior distribution obtained in the flexible six-parameter realization is broadly centered around $n \sim \mathcal{O}(1)$, corresponding to $p \sim \mathcal{O}(1\text{--}3)$ through the relation $p = 3/n$. Current data, therefore, do not isolate a unique curvature class of the scalar potential, but remain consistent with a broad

family of analytic minima, including the canonical quartic symmetry-breaking case as well as flatter realizations.

In this regime, the likelihood manifold contains an approximately flat direction along which compensating variations preserve consistency between geometric and growth observables. Fixing $n = 3$ removes this functional degree of freedom. The resulting model remains geometrically viable and provides an acceptable fit to SN distances, but the posterior manifold becomes more anisotropic under the combined Planck+RSD+SN constraint. Marginalized distributions contract and shift toward prior boundaries, partly reflecting truncation where the degeneracy direction extends beyond the adopted prior range, without any corresponding improvement in χ^2 . This truncation indicates that the degeneracy direction present in the flexible realization extends toward parameter values slightly outside the adopted prior domain once the activation index is fixed, rather than representing a purely data-driven contraction of the likelihood surface. The principal conclusion is therefore structural rather than statistical.

A sufficient degree of functional flexibility in the interaction history, therefore, allows the model to remain observationally viable while preserving perturbative consistency. Reducing this dimensionality does not immediately lead to catastrophic disagreement with the data, but it compresses the allowed parameter volume and removes interior degeneracy directions. Current observations, therefore, provide limited constraints on the dimensional structure of the interaction history, favoring models in which the redshift dependence of the coupling retains at least one continuous degree of freedom. This observation provides guidance for constructing consistent scalar realizations of late-time dark sector interactions and clarifies which aspects of the activation mechanism are presently testable. Dynamical consistency of the posterior solutions with the adiabatic hierarchy is examined in Appendix A.

7 Structural Interpretation of Observational Constraints

7.1 Observational Position of the Scalar-Tensor Theory in Microscopic Parameter Space

The observational analysis of Sec. 6 shows that the interacting realization remains statistically consistent with Λ CDM across all dataset combinations, with posterior support confined to the perturbative regime defined in Sec. 2.3. This empirical result can be translated into a statement about the location of the theory within its microscopic parameter space.

In the controlled tracking regime, deviations of the DM dilution law from the standard scaling are governed by the dimensionless parameter $\varepsilon(a)$ introduced in Eq. (2.23). Using the adiabatic scaling relation (2.27), the deformation amplitude can be written as

$$\varepsilon(a) \sim 3\beta^2(\phi) \frac{H^2(a)}{m_{\text{eff}}^2(a)}, \quad (7.1)$$

where $m_{\text{eff}}^2 = \partial^2 V_{\text{eff}} / \partial \phi^2$ is evaluated along the density-controlled attractor trajectory.

The perturbative consistency requirement of Eq. (2.31) restricts $|\varepsilon|$ to remain below the percent level over the redshift interval probed by current observations. The most restrictive condition typically occurs near the activation epoch $a = a_c$, where the effective coupling varies most rapidly. Using the logistic activation profile of Eq. (4.6), one has $\beta(a_c) = \beta_0/2$.

Evaluating Eq. (7.1) at $a = a_c$ then gives

$$\varepsilon(a_c) = \frac{9}{4} \beta_0^2 \frac{H^2(a_c)}{m_{\text{eff}}^2(a_c)}. \quad (7.2)$$

Applying the observational bound (2.31) implies

$$\frac{9}{4} \beta_0^2 \frac{H^2(a_c)}{m_{\text{eff}}^2(a_c)} \lesssim 10^{-2}, \quad (7.3)$$

or equivalently

$$m_{\text{eff}}(a_c) \gtrsim \mathcal{O}(10) \beta_0 H(a_c). \quad (7.4)$$

Equation (7.4) provides a simple microscopic interpretation of the observational null result. Current data place the theory in a region of parameter space where the scalar mass at activation exceeds the Hubble scale by at least an order of magnitude (for $\beta_0 \sim \mathcal{O}(1)$), such that $m_{\text{eff}}^2 \gg H^2$. The field therefore resides deep within the adiabatic tracking regime, where background deformations remain perturbatively small, and the logistic reduction operates within its domain of validity. The Λ CDM limit $\beta_0 \rightarrow 0$ corresponds smoothly to $m_{\text{eff}}^2/H^2 \rightarrow \infty$ and thus lies well inside the allowed microscopic region. Current observations thus do not exclude the scalar-tensor realization of IDE, but instead confine the theory to a hierarchical sector of parameter space characterized by a heavy scalar relative to the Hubble scale and a perturbatively small effective coupling over the cosmologically relevant epoch.

7.2 Structural Meaning of Degeneracy Compression

A clear qualitative distinction emerges between the flexible realization (free n) and the fixed-index case ($n = 3$). While the six-parameter model retains extended posterior support, the fixed-index realization exhibits boundary accumulation and pronounced anisotropy in parameter space. Part of this accumulation reflects truncation, where the degeneracy direction extends beyond the adopted prior range once the activation index is fixed. This behavior reflects a structural property of the interaction sector rather than a numerical artifact of the sampling procedure. The activation index n inferred from the data can be interpreted through the microphysical relation $n = 3/p$, where p is the order of the first nonvanishing derivative of $V'(\phi)$ at the symmetry-breaking minimum. The posterior region $n \in [n_{\text{min}}, n_{\text{max}}]$ therefore corresponds to curvature classes $p \approx 3/n$. For example, the canonical quartic potential corresponds to $p = 1$ ($n = 3$), while flatter minima with $p > 1$ produce smaller values of n . Current constraints are consistent with $n \approx 3$, indicating compatibility with a non-degenerate analytic minimum, although flatter potentials remain allowed within uncertainties.

When n is free, the model possesses a continuous shape degree of freedom that redistributes the interaction strength across redshift while maintaining perturbative consistency of the background evolution. This additional direction in parameter space absorbs the combined geometric and growth constraints, maintaining extended posterior support and statistical compatibility with Λ CDM. Fixing n removes this functional freedom, rigidly specifying the activation history. The remaining freedom is then limited primarily to amplitude parameters such as Ω_m , β_0 , a_c , while γ

serves as a derived diagnostic of the perturbative background arising from the adiabatic reduction of the coupled DM–scalar dynamics (see Appendix B). Under the combined Planck+RSD+SN constraints, these parameters alone cannot accommodate the joint likelihood without driving solutions toward prior boundaries. The resulting degeneracy compression, therefore, reflects a loss of functional flexibility rather than evidence for a preferred nonzero coupling.

This behavior is consistent with the microscopic positioning derived above. Because observations confine the theory to the perturbative regime $|\varepsilon| \ll 1$, modifications to the homogeneous expansion remain small and observational sensitivity therefore arises primarily through subtle growth–geometry interplay. In this regime, functional freedom in the activation history becomes statistically important. Fixing the activation profile removes this flexibility and sharpens curvature in the likelihood surface without improving goodness-of-fit, indicating over-restriction rather than physical detection. The observational outcome, therefore, admits a clear structural interpretation: density-driven IDE remains viable within the perturbative hierarchical regime, but viable realizations must retain sufficient flexibility in the redshift dependence of the activation mechanism to satisfy combined geometric and growth constraints.

8 Discussion

8.1 Implications for scalar-tensor IDE models

The central result of this work is that current cosmological data exhibit discernible sensitivity to the functional form of dark sector interactions, even when the overall coupling amplitude remains consistent with zero. In our construction, the redshift dependence of the interaction is not imposed phenomenologically but emerges dynamically from the evolution of a scalar field toward a density-controlled minimum of the effective potential. The activation index n governing this profile is therefore not a free fitting parameter; rather, it is determined by the local restoring structure of the scalar potential through $n = 3/p$, where p denotes the order of the first nonvanishing derivative of $V'(\phi)$ at the minimum. Observational constraints on n thus provide an indirect probe of the curvature of the underlying symmetry-breaking potential, translating large-scale structure measurements into microphysical information about the dark sector.

Parameter inference reveals that allowing n to vary preserves an extended interior posterior region, whereas fixing the canonical value $n = 3$ (corresponding to a minimal quartic potential) removes this degeneracy direction and compresses the posterior volume without improving the likelihood. This behavior indicates that viable scalar–tensor realizations of IDE may require greater functional flexibility than the simplest symmetry-breaking minimum affords. The posterior distribution of the activation index remains broadly centered around $n \sim \mathcal{O}(1)$, which translates into a curvature class $p = 3/n \sim \mathcal{O}(1-3)$ for the underlying scalar potential. Current observations are therefore compatible with a broad family of analytic symmetry-breaking minima, ranging from the canonical quartic case ($p = 1$) to moderately flatter realizations ($p > 1$), and do not yet isolate a unique microscopic curvature class. This means that, while the data do not require a departure from the quartic potential, they also do not disfavor richer structures, leaving the precise restoring order of the scalar sector undetermined within current uncertainties.

8.2 Implications for phenomenological IDE models

A key feature of the present framework is that the interaction arises from a covariant scalar-tensor theory rather than from a phenomenological background ansatz. In many IDE models, the energy transfer term is introduced directly at the level of the continuity equations with freely chosen amplitude and redshift dependence. In such approaches, the direction of energy exchange, the magnitude of the background deformation, and the growth-sector modification are treated as largely independent degrees of freedom.

In the scalar-tensor realization considered here, these quantities are dynamically linked. The interaction originates from the motion of the scalar field toward the density-dependent minimum of the effective potential, and stability of this minimum requires $m_{\text{eff}}^2 > 0$. The strength of the induced background deformation is therefore controlled by the microscopic ratio $\beta_0^2/m_{\text{eff}}^2$ evaluated near the activation epoch, rather than by an arbitrary coupling parameter. The observational requirement that deviations from the standard matter dilution law remain small ($|\epsilon| < 10^{-2}$) forces this ratio to be small, implying $m_{\text{eff}} \gtrsim \mathcal{O}(10)\beta_0 H$ near activation.

In this regime, the scalar rapidly relaxes toward the density-controlled minimum as the cosmic matter density evolves. The interaction, therefore, does not vanish but remains perturbatively suppressed, producing small corrections to the matter dilution law and to the growth of structure while leaving the background expansion close to Λ CDM. The scalar-tensor IDE construction thus occupies a constrained region of the broader phenomenological IDE parameter space, in which the interaction amplitude, the direction of energy flow, and the magnitude of background deformation are tied to microscopic stability conditions of the scalar sector.

8.3 Future prospects

Upcoming cosmological surveys—most notably Euclid [83], the Vera C. Rubin Observatory’s Legacy Survey of Space and Time (LSST), and the Nancy Grace Roman Space Telescope [84] are expected to improve measurements of the growth observable $f\sigma_8(z)$ substantially [85]. An increased precision will tighten constraints on the hierarchy m_{eff}/H that governs the interaction strength in the scalar–tensor realization considered here. Even if the coupling amplitude β_0 remains undetectably small, improved growth measurements may allow discrimination between different curvature classes of the scalar potential, corresponding to different values of the activation index n .

Looking beyond the perturbative regime, a systematic investigation of the limit $m_{\text{eff}} \sim H$ would clarify where the adiabatic tracking approximation breaks down and reveal whether qualitatively new dynamics emerge as the scalar mass approaches the Hubble scale. Embedding the present mechanism within the EFT of dark energy [9, 86] could further connect the activation index n to broader classes of scalar–tensor interactions, enabling systematic differentiation between possible microscopic realizations. Together, these observational and theoretical directions will determine how tightly the structurally constrained manifold of density-driven IDE can be probed beyond the perturbative tracking regime.

8.4 Conclusion

We have shown that density-driven symmetry breaking in a scalar–tensor theory naturally generates a logistic activation profile for the dark sector coupling, with the activation index determined

by the local restoring order of the scalar potential. Confronting this parametrization with Planck CMB lensing, redshift-space distortions, and Pantheon+SH0ES supernova data, we find that the scenario lies well within the adiabatic tracking regime. In this regime, the combined geometric and growth constraints reveal sensitivity to the functional form of the interaction. Allowing the activation index to vary preserves an extended posterior region, whereas fixing it to its canonical value corresponding to a minimal quartic potential reduces posterior degeneracy without improving the quality of fit. The corresponding curvature class of the scalar potential indicates that current observations remain compatible with a broad family of analytic symmetry-breaking minima, including the canonical quartic case as well as moderately flatter potentials.

Regarding the current cosmological tensions, our analysis yields a clear negative result. The H_0 tension remains unaffected by construction, while the S_8 tension shows negligible correlation with the interaction parameters, indicating that this class of models cannot resolve the clustering discrepancy. The significance of the analysis, therefore, lies elsewhere: growth data from RSD provide the dominant leverage on the interaction sector, with geometric data mainly serving to break degeneracies in the baseline cosmological parameters. Even in the absence of a detectable coupling amplitude, present data already probe the structural flexibility of the activation mechanism, translating observational constraints into a microphysical requirement near the transition epoch. Future surveys such as Euclid, Rubin/LSST, and Roman will determine how tightly this constrained manifold can be tested beyond the perturbative tracking regime.

9 Acknowledgements

PKMV, KNS, and KA acknowledge that part of the numerical computations presented in this work were carried out using the Pegasus computing cluster at IUCAA, Pune, India. PKMV acknowledges financial support from the Seed Money Scheme of CHRIST (Deemed to be University) under Sanction No. CU-ORS-SM-24/29.

A Early-Time Asymptotics and Adiabatic Consistency

In this Appendix, we derive the analytic high-redshift behavior of the adiabatic mass hierarchy introduced in Sec. 2 and verify that the posterior solutions obtained in Sec. 6 remain within the adiabatic tracking regime over the observationally relevant redshift range.

A.1 Effective mass along the density-controlled trajectory

The effective mass governing small fluctuations about the density-controlled minimum is defined as

$$m_{\text{eff}}^2 = \left. \frac{\partial^2 V_{\text{eff}}}{\partial \phi^2} \right|_{\phi=\phi_{\text{ad}}}, \quad (\text{A.1})$$

where V_{eff} is given in Eq. (2.16). For the polynomial family $V(\phi) = -\frac{1}{2}\mu^2\phi^2 + \frac{\lambda}{2m}\phi^{2m}$, one obtains

$$m_{\text{eff}}^2 = -\mu^2 + \lambda(2m-1)\phi_{\text{ad}}^{2m-2}. \quad (\text{A.2})$$

Using the vacuum relation $v^{2m-2} = \mu^2/\lambda$ and defining the dimensionless ratio $x \equiv \phi_{\text{ad}}/v$, Eq. (A.2) becomes

$$m_{\text{eff}}^2 = \mu^2 [(2m-1)x^{2m-2} - 1]. \quad (\text{A.3})$$

Along the adiabatic tracking trajectory, the algebraic balance condition (2.19) reads

$$x^{2m-1} - x = \xi(a), \quad \xi(a) = \xi_0 a^{-3}, \quad (\text{A.4})$$

where we have used the controlled perturbative scaling $\rho_{\text{DM}} \propto a^{-3}$ established in Sec. 2.3 and $\xi(a)$ takes the form defined in Eq. (2.18).

A.2 High-redshift asymptotics

At sufficiently high redshift ($a \ll 1$), the Universe is matter-dominated and

$$H^2(a) \simeq H_0^2 \Omega_m a^{-3}. \quad (\text{A.5})$$

In this regime $\xi(a) \gg 1$, so Eq. (A.4) is dominated by the highest-power term,

$$x^{2m-1} \simeq \xi_0 a^{-3}. \quad (\text{A.6})$$

Hence,

$$x(a) \simeq \xi_0^{1/(2m-1)} a^{-3/(2m-1)}. \quad (\text{A.7})$$

Substituting Eq. (A.7) into Eq. (A.3) and retaining the leading contribution at large x , we obtain

$$m_{\text{eff}}^2 \simeq \mu^2 (2m-1) \xi_0^{\frac{2m-2}{2m-1}} a^{-\frac{3(2m-2)}{2m-1}}. \quad (\text{A.8})$$

Dividing by Eq. (A.5), the hierarchy ratio becomes

$$\frac{m_{\text{eff}}^2}{H^2} \simeq \frac{\mu^2}{H_0^2} \frac{(2m-1)}{\Omega_m} \xi_0^{\frac{2m-2}{2m-1}} a^{\frac{3}{2m-1}}. \quad (\text{A.9})$$

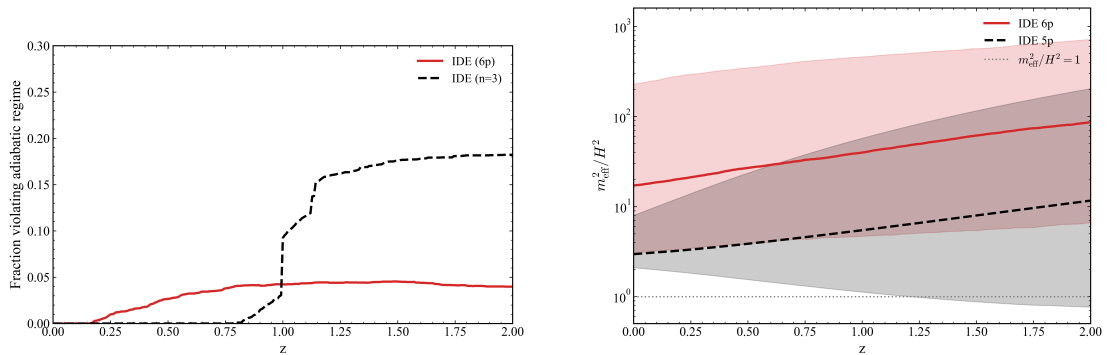
Thus, the universal early-time scaling is

$$\frac{m_{\text{eff}}^2}{H^2} \propto a^{\frac{3}{2m-1}} = (1+z)^{-\frac{3}{2m-1}}. \quad (\text{A.10})$$

Since $2m-1 > 0$, the exponent is positive and therefore

$$\lim_{z \rightarrow \infty} \frac{m_{\text{eff}}^2}{H^2} = 0. \quad (\text{A.11})$$

The above equation shows that the strict adiabatic hierarchy $m_{\text{eff}}^2 \gg H^2$ cannot hold for arbitrarily long times in the past. At sufficiently high redshift, Hubble friction grows faster than the curvature of the density-shifted minimum, and the system transitions from algebraic tracking to a Hubble-drag dominated regime. The logistic normal form derived in Sec. 3 therefore describes the late-time attractor and is not intended as an exact early-time solution. This breakdown at high redshift is expected and does not affect the analysis, since the logistic parametrization is applied only over the redshift range $z \lesssim 2$ where the hierarchy remains valid.



(a) Redshift evolution of the fraction of posterior samples violating the adiabatic condition $m_{\text{eff}}^2/H^2 > 1$.

(b) Median and 68% credible region of m_{eff}^2/H^2 .

Figure 7: Adiabatic tracking diagnostics from Planck+RSD+SN posterior samples. *Left:* fraction of samples violating $m_{\text{eff}}^2/H^2 > 1$. *Right:* median and 68% credible interval of m_{eff}^2/H^2 . The ratio decreases toward high redshift, consistent with Eq. (A.10). Over $0 \leq z \leq 2$, solutions remain predominantly adiabatic, validating the tracking approximation.

A.3 Consistency over the observational window

Cosmological observations constrain the expansion and growth history primarily over the interval $0 \lesssim z \lesssim 2$. To verify that the posterior solutions analyzed in Sec. 6 remain within the regime assumed in Sec. 2.1, we reconstruct the ratio m_{eff}^2/H^2 using the full MCMC chains for each accepted parameter vector. Figure 7 shows (i) the redshift evolution of the fraction of posterior samples violating the adiabatic condition $m_{\text{eff}}^2/H^2 > 1$, and (ii) the median and 68% credible region of the hierarchy ratio for the Planck+RSD+SN dataset combination.

At $z = 0$, all viable posterior samples satisfy $m_{\text{eff}}^2/H^2 > 1$. Over the interval $0 \leq z \leq 2$, the median trajectory and the central posterior region remain within the adiabatic regime. A minority of samples approach the boundary $m_{\text{eff}}^2/H^2 \simeq 1$ near the upper end of the redshift interval, but no systematic breakdown of the hierarchy is observed within the observational window. It is important to distinguish this adiabatic consistency condition from the perturbative energy-exchange bound imposed in Sec. 2.3. The hierarchy $m_{\text{eff}}^2/H^2 \gg 1$ controls the validity of the algebraic tracking reduction, whereas the bound $|\mathcal{E}(a)| < \mathcal{E}_*$ ensures that the cumulative background deformation remains small. The two conditions are related but logically distinct.

B Origin of the Background Deformation Parameter

This appendix derives the effective background deformation parameter γ that characterizes the integrated effect of the dark sector interaction on the matter dilution law. While the main analysis adopts a Λ CDM background within the controlled perturbative regime (Sec. 2.3), the scalar–tensor interaction generically induces a small modification to $\rho_{\text{DM}}(a)$ through energy exchange with the scalar field. Starting from the exact covariant equations, we show how γ emerges

from the microscopic quantities $(\beta_0, m_{\text{eff}})$ and demonstrate that the resulting deformation of the expansion history remains safely below current observational uncertainties when $|\gamma| \ll 1$.

B.1 From covariant dynamics to the reduced continuity equation

The exact DM continuity equation in the Einstein frame (c.f. Eq. (2.5)) is given by [87, 88],

$$\dot{\rho}_{\text{DM}} + 3H\rho_{\text{DM}} = -\frac{\beta(\phi)}{M_{\text{Pl}}}\dot{\phi}\rho_{\text{DM}}. \quad (\text{B.1})$$

In the adiabatic tracking regime (Sec. 2.1), the scalar field follows the density-controlled minimum determined by Eq. (2.10). Differentiating this condition with respect to time and using the definition of the effective mass,

$$m_{\text{eff}}^2(\phi_{\text{ad}}) \equiv \left. \frac{\partial^2 V_{\text{eff}}}{\partial \phi^2} \right|_{\phi=\phi_{\text{ad}}}, \quad (\text{B.2})$$

yields a relation between $\dot{\phi}$ and $\dot{\rho}_{\text{DM}}$:

$$m_{\text{eff}}^2(\phi_{\text{ad}})\dot{\phi} = \frac{\beta(\phi_{\text{ad}})}{M_{\text{Pl}}}\dot{\rho}_{\text{DM}}. \quad (\text{B.3})$$

Within the controlled perturbative regime, the energy exchange remains small compared to Hubble dilution, so that to leading order $\dot{\rho}_{\text{DM}} \simeq -3H\rho_{\text{DM}}$. Substituting this approximation into Eq. (B.3) gives an expression for the field velocity,

$$\dot{\phi} = -3H\frac{\beta(\phi)\rho_{\text{DM}}}{M_{\text{Pl}}m_{\text{eff}}^2}. \quad (\text{B.4})$$

Inserting Eq. (B.4) back into the continuity equation (B.1) eliminates the explicit scalar field dynamics and yields a closed equation for the matter density [47]:

$$\dot{\rho}_{\text{DM}} + 3H\rho_{\text{DM}} = 3H\frac{\beta^2(\phi)\rho_{\text{DM}}^2}{M_{\text{Pl}}^2 m_{\text{eff}}^2}. \quad (\text{B.5})$$

In logarithmic form, this becomes

$$\frac{d\rho_{\text{DM}}}{d\ln a} = -3\rho_{\text{DM}} + 3\frac{\beta^2(\phi)\rho_{\text{DM}}^2}{M_{\text{Pl}}^2 m_{\text{eff}}^2}. \quad (\text{B.6})$$

It is convenient to introduce the dimensionless interaction parameter already defined in Sec. 2.3,

$$\varepsilon(a) \equiv \frac{3\beta^2(\phi)\rho_{\text{DM}}}{M_{\text{Pl}}^2 m_{\text{eff}}^2}, \quad (\text{B.7})$$

in terms of which Eq. (B.6) simplifies to

$$\frac{d\rho_{\text{DM}}}{d\ln a} = -3\rho_{\text{DM}}(1 - \varepsilon(a)). \quad (\text{B.8})$$

For a stable tracking branch, $m_{\text{eff}}^2 > 0$ implies $\varepsilon(a) > 0$; the interaction therefore slows matter dilution relative to the standard a^{-3} scaling.

B.2 Mapping to the logistic activation profile

The logistic form of the coupling derived in Sec. 4,

$$\beta(a) = \beta_0 \frac{a^n}{a^n + a_c^n}, \quad (\text{B.9})$$

allows us to express the interaction parameter as

$$\varepsilon(a) = \frac{3\beta_0^2 x(a)^2 \rho_{\text{DM}}}{M_{\text{Pl}}^2 m_{\text{eff}}^2}, \quad x(a) \equiv \frac{a^n}{a^n + a_c^n}. \quad (\text{B.10})$$

Near the activation epoch $a = a_c$, the ratio $\rho_{\text{DM}}/m_{\text{eff}}^2$ varies slowly compared to the rapid turn-on of $x(a)$. Expanding about a_c and keeping the leading contribution gives

$$\varepsilon(a) \simeq \varepsilon_c x(a)^2, \quad \varepsilon_c \equiv \frac{3\beta_0^2 \rho_{\text{DM}}(a_c)}{M_{\text{Pl}}^2 m_{\text{eff}}^2(a_c)}. \quad (\text{B.11})$$

The evolution equation (B.8) then reduces locally to

$$\frac{d\rho_{\text{DM}}}{d \ln a} = -3\rho_{\text{DM}} + 3\varepsilon_c x(a)^2 \rho_{\text{DM}}. \quad (\text{B.12})$$

To leading order in the perturbative regime, the quadratic activation profile can be approximated by an equivalent linear form that reproduces the same fixed points and local slope near the activation epoch. Writing

$$\frac{d\rho_{\text{DM}}}{d \ln a} = -3\rho_{\text{DM}} - \gamma x(a) \rho_{\text{DM}}, \quad (\text{B.13})$$

we identify the effective deformation parameter

$$\gamma = -3\varepsilon_c = -\frac{9\beta_0^2 \rho_{\text{DM}}(a_c)}{M_{\text{Pl}}^2 m_{\text{eff}}^2(a_c)}. \quad (\text{B.14})$$

Equation (B.14) shows that γ is directly proportional to the interaction strength evaluated at the activation epoch. The perturbative condition $|\varepsilon(a)| \ll 1$ ensures that $|\gamma| \ll 1$, which keeps the induced background deformation small. Furthermore, when $\varepsilon_c > 0$, the sign of γ is negative, indicating that the interaction effectively reduces the dilution rate.

C Declaration of Generative AI and AI-assisted technologies in the writing process

During the preparation of this work, the author, Pradosh Keshav MV, utilized Grammarly/ChatGPT-5 to correct grammatical mistakes and enhance the structure of specific paragraphs. After using this tool/service, the author reviewed and edited the content as needed and takes full responsibility for the content of the publication.

References

- [1] Adam G Riess, Wenlong Yuan, Lucas M Macri, Dan Scolnic, Dillon Brout, Stefano Casertano, David O Jones, Yukei Murakami, Gagandeep S Anand, Louise Breuval, et al. A comprehensive measurement of the local value of the hubble constant with 1 km s⁻¹ mpc⁻¹ uncertainty from the hubble space telescope and the sh0es team. *The Astrophysical journal letters*, 934(1):L7, 2022.
- [2] Peter AR Ade, N Aghanim, M Arnaud, M Ashdown, J Aumont, C Baccigalupi, AJ Banday, RB Barreiro, Nicola Bartolo, E Battaner, et al. Planck 2015 results-xiv. dark energy and modified gravity. *Astronomy & Astrophysics*, 594:A14, 2016.
- [3] Miguel A Sabogal, Emanuely Silva, Rafael C Nunes, Suresh Kumar, and Eleonora Di Valentino. Sign switching in dark sector coupling interactions as a candidate for resolving cosmological tensions. *Physical Review D*, 111(4):043531, 2025.
- [4] Catherine Heymans, Tilman Tröster, Marika Asgari, Chris Blake, Hendrik Hildebrandt, Benjamin Joachimi, Konrad Kuijken, Chieh-An Lin, Ariel G Sánchez, Jan Luca Van Den Busch, et al. Kids-1000 cosmology: Multi-probe weak gravitational lensing and spectroscopic galaxy clustering constraints. *Astronomy & Astrophysics*, 646:A140, 2021.
- [5] Nabila Aghanim, Yashar Akrami, Mark Ashdown, Jonathan Aumont, Carlo Baccigalupi, Mario Ballardini, Anthony J Banday, RB Barreiro, Nicola Bartolo, S Basak, et al. Planck 2018 results-vi. cosmological parameters. *Astronomy & Astrophysics*, 641:A6, 2020.
- [6] Meng-Xiang Lin, Bhuvnesh Jain, Marco Raveri, Eric J Baxter, Chihway Chang, Marco Gatti, Sujeong Lee, and Jessica Muir. Late time modification of structure growth and the s 8 tension. *Physical Review D*, 109(6):063523, 2024.
- [7] Miguel A Sabogal, Emanuely Silva, Rafael C Nunes, Suresh Kumar, Eleonora Di Valentino, and William Giarè. Quantifying the s 8 tension and evidence for interacting dark energy from redshift-space distortion measurements. *Physical Review D*, 110(12):123508, 2024.
- [8] Adam Smith, Maria Mylova, Philippe Brax, Carsten van de Bruck, CP Burgess, and Anne-Christine Davis. A minimal axio-dilaton dark sector. *Journal of Cosmology and Astroparticle Physics*, 2025(07):023, 2025.
- [9] Jérôme Gleyzes, David Langlois, Michele Mancarella, and Filippo Vernizzi. Effective theory of interacting dark energy. *Journal of Cosmology and Astroparticle Physics*, 2015(08):054, 2015.
- [10] Jérôme Gleyzes, David Langlois, Michele Mancarella, and Filippo Vernizzi. Effective theory of dark energy at redshift survey scales. *Journal of Cosmology and Astroparticle Physics*, 2016(02):056, 2016.
- [11] Luca Amendola. Coupled quintessence. *Physical Review D*, 62(4):043511, 2000.
- [12] Christof Wetterich. Cosmology and the fate of dilatation symmetry. *Nuclear Physics B*, 302(4):668–696, 1988.
- [13] R. Bean, E. E. Flanagan, I. Laszlo, and M. Trodden. Constraining Interactions in Cosmology’s Dark Sector. *Phys. Rev. D*, 78:123514, 2008.
- [14] Guido D’Amico, Teresa Hamill, and Nemanja Kaloper. Quantum field theory of interacting dark matter and dark energy: Dark monodromies. *Physical Review D*, 94(10):103526, 2016.
- [15] Alkistis Poursidou, C Skordis, and EJ Copeland. Models of dark matter coupled to dark energy. *Physical Review D—Particles, Fields, Gravitation, and Cosmology*, 88(8):083505, 2013.

- [16] Eleonora Di Valentino, Alessandro Melchiorri, Olga Mena, Supriya Pan, and Weiqiang Yang. Interacting dark energy in a closed universe. *Monthly Notices of the Royal Astronomical Society: Letters*, 502(1):L23–L28, 2021.
- [17] Weiqiang Yang, Ankan Mukherjee, Eleonora Di Valentino, and Supriya Pan. Interacting dark energy with time varying equation of state and the h_0 tension. *Physical Review D*, 98(12):123527, 2018.
- [18] Bin Wang, Elcio Abdalla, Fernando Atrio-Barandela, and Diego Pavon. Further understanding the interaction between dark energy and dark matter: current status and future directions. *Reports on Progress in Physics*, 2024.
- [19] Jussi Väliviita, Elisabetta Majerotto, and Roy Maartens. Large-scale instability in interacting dark energy and dark matter fluids. *Journal of Cosmology and Astroparticle Physics*, 2008(07):020, 2008.
- [20] J. H. He and B. Wang. Effects of the interaction between dark energy and dark matter on cosmological parameters. *JCAP*, 0806:010, 2008.
- [21] Thibault Damour, GW Gibbons, and C Gundlach. Dark matter, time-varying g , and a dilaton field. *Physical review letters*, 64(2):123, 1990.
- [22] Thibault Damour and Alexander M Polyakov. The string dilation and a least coupling principle. *Nuclear Physics B*, 423(2-3):532–558, 1994.
- [23] Maurizio Gasperini and Gabriele Veneziano. Dilaton production in string cosmology. *Physical Review D*, 50(4):2519, 1994.
- [24] Brian Patt and Frank Wilczek. Higgs-field portal into hidden sectors. *arXiv preprint hep-ph/0605188*, 2006.
- [25] Andrey Katz and Maxim Perelstein. Higgs couplings and electroweak phase transition. *Journal of High Energy Physics*, 2014(7):1–24, 2014.
- [26] David Curtin and Shayne Gryba. Twin higgs portal dark matter. *Journal of High Energy Physics*, 2021(8):1–45, 2021.
- [27] Taeil Hur, Dong-Won Jung, Pyungwon Ko, and Jae Yong Lee. Electroweak symmetry breaking and cold dark matter from strongly interacting hidden sector. *Physics Letters B*, 696(3):262–265, 2011.
- [28] K Bamba, R Gannouji, M Kamijo, S Nojiri, and M Sami. Spontaneous symmetry breaking in cosmos: The hybrid symmetron as a dark energy switching device. *Journal of Cosmology and Astroparticle Physics*, 2013(07):017, 2013.
- [29] Kalliopi Petraki, Lauren Pearce, and Alexander Kusenko. Self-interacting asymmetric dark matter coupled to a light massive dark photon. *Journal of Cosmology and Astroparticle Physics*, 2014(07):039, 2014.
- [30] Justin Khoury and Amanda Weltman. Chameleon fields: Awaiting surprises for tests of gravity in space. *Physical review letters*, 93(17):171104, 2004.
- [31] Kurt Hinterbichler and Justin Khoury. Screening long-range forces through local symmetry restoration. *Physical review letters*, 104(23):231301, 2010.
- [32] Amol Upadhye. Symmetron dark energy in laboratory experiments. *Physical review letters*, 110(3):031301, 2013.

- [33] Alexei A Starobinsky. Disappearing cosmological constant in $f(r)$ gravity. *JETP letters*, 86(3):157–163, 2007.
- [34] Ignacy Sawicki, Ippocratis D Saltas, Luca Amendola, and Martin Kunz. Consistent perturbations in an imperfect fluid. *Journal of Cosmology and Astroparticle Physics*, 2013(01):004, 2013.
- [35] Özgür Akarsu, Eoin Ó Colgáin, Anjan A Sen, and MM Sheikh-Jabbari. λ cdm tensions: localising missing physics through consistency checks. *Universe*, 10(8):305, 2024.
- [36] George Alestas and Leandros Perivolaropoulos. Late-time approaches to the hubble tension deforming $h(z)$, worsen the growth tension. *Monthly Notices of the Royal Astronomical Society*, 504(3):3956–3962, 2021.
- [37] David Benisty, Supriya Pan, Denitsa Staicova, Eleonora Di Valentino, and Rafael C Nunes. Late-time constraints on interacting dark energy: Analysis independent of h_0 , r_d , and m_b . *Astronomy & Astrophysics*, 688:A156, 2024.
- [38] Pradosh Keshav MV, NS Kavya, and Kenath Arun. Spontaneous symmetry breaking as a late-time trigger for interacting dark energy. *arXiv preprint arXiv:2511.14235*, 2025.
- [39] Pradosh Keshav M. V. and Arun Kenath. Quintessence and false vacuum: Two sides of the same coin? *Pramana*, 99(2):58, 2025.
- [40] Felipe Avila, Armando Bernui, Alexander Bonilla, and Rafael C Nunes. Inferring $s_8(z)$ and $\gamma(z)$ with cosmic growth rate measurements using machine learning. *The European Physical Journal C*, 82(7):594, 2022.
- [41] PantheonPlusSH0ES Collaboration. PantheonplussH0es datarelease: Pantheon+ data. https://github.com/PantheonPlusSH0ES/DataRelease/tree/main/Pantheon%2B_Data, October 2022. Accessed: 2025-08-14.
- [42] Thibault Damour and Gilles Esposito-Farese. Tensor-multi-scalar theories of gravitation. *Classical and Quantum Gravity*, 9(9):2093–2176, 1992.
- [43] Valerio Faraoni. Scalar-tensor gravity. In *Cosmology in Scalar-Tensor Gravity*, pages 1–53. Springer, 2004.
- [44] Timothy Clemson, Kazuya Koyama, Gong-Bo Zhao, Roy Maartens, and Jussi Väliviita. Interacting dark energy: Constraints and degeneracies. *Physical Review D—Particles, Fields, Gravitation, and Cosmology*, 85(4):043007, 2012.
- [45] Miguel Zumalacárregui and Juan García-Bellido. Transforming gravity: from derivative couplings to matter to second-order scalar-tensor theories beyond the horndeski lagrangian. *Physical Review D*, 89(6):064046, 2014.
- [46] Tomi S Koivisto, David F Mota, and Miguel Zumalacárregui. Screening modifications of gravity through disformally coupled fields. *Physical review letters*, 109(24):241102, 2012.
- [47] Philippe Brax, Anne-Christine Davis, Baojiu Li, and Hans A Winther. Unified description of screened modified gravity. *Physical Review D—Particles, Fields, Gravitation, and Cosmology*, 86(4):044015, 2012.
- [48] Kurt Hinterbichler, Justin Khoury, Aaron Levy, and Andrew Matas. Symmetron cosmology. *Physical Review D—Particles, Fields, Gravitation, and Cosmology*, 84(10):103521, 2011.
- [49] Abdolali Banihashemi, Nima Khosravi, and Amir H Shirazi. Ginzburg-landau theory of dark energy: a framework to study both temporal and spatial cosmological tensions simultaneously. *Physical Review D*, 99(8):083509, 2019.

- [50] Fred C Adams. General solutions for tunneling of scalar fields with quartic potentials. *Physical Review D*, 48(6):2800, 1993.
- [51] Christopher W Murphy. Nlo perturbativity bounds on quartic couplings in renormalizable theories with ϕ^4 -like scalar sectors. *Physical Review D*, 96(3):036006, 2017.
- [52] Christiane Quesne. Quasi-exactly solvable symmetrized quartic and sextic polynomial oscillators. *The European Physical Journal Plus*, 132(11):450, 2017.
- [53] Howard Georgi. Effective field theory. *Annual review of nuclear and particle science*, 43(1):209–252, 1993.
- [54] Hai-Chao Zhang. Obtaining a scalar fifth force via a symmetry-breaking coupling between the scalar field and matter. *Physical Review D*, 101(4):044020, 2020.
- [55] Shadab Alam, Arnaud De Mattia, Amélie Tamone, S Avila, John A Peacock, V Gonzalez-Perez, Alex Smith, Anand Raichoor, Ashley J Ross, Julian E Bautista, et al. The completed sdss-iv extended baryon oscillation spectroscopic survey: N-body mock challenge for the eboss emission line galaxy sample. *Monthly Notices of the Royal Astronomical Society*, 504(4):4667–4686, 2021.
- [56] Kwan Chuen Chan, S Avila, A Carnero Rosell, I Ferrero, J Elvin-Poole, E Sanchez, H Camacho, A Porredon, M Crocce, TMC Abbott, et al. Dark energy survey year 3 results: Measurement of the baryon acoustic oscillations with three-dimensional clustering. *Physical Review D*, 106(12):123502, 2022.
- [57] Jaime Ruiz-Zapatero, Carlos Garcia-Garcia, David Alonso, Pedro G Ferreira, and Richard DP Grumitt. Model-independent constraints on Ω_m and $h(z)$ from the link between geometry and growth. *Monthly Notices of the Royal Astronomical Society*, 512(2):1967–1984, 2022.
- [58] Steven H Strogatz. *Nonlinear dynamics and chaos: with applications to physics, biology, chemistry, and engineering*. Chapman and Hall/CRC, 2024.
- [59] Edmund J Copeland, Andrew R Liddle, and David Wands. Exponential potentials and cosmological scaling solutions. *Physical Review D*, 57(8):4686, 1998.
- [60] E. J. Copeland, M. Sami, and S. Tsujikawa. Dynamics of Dark Energy. *Int. J. Mod. Phys. D*, 15:1753–1936, 2006.
- [61] Eric V Linder. Reconstructing and deconstructing dark energy. *Physical Review D—Particles, Fields, Gravitation, and Cosmology*, 70(6):061302, 2004.
- [62] Eric V Linder and Dragan Huterer. How many dark energy parameters? *Physical Review D—Particles, Fields, Gravitation, and Cosmology*, 72(4):043509, 2005.
- [63] Eleonora Di Valentino, Alessandro Melchiorri, Eric V Linder, and Joseph Silk. Constraining dark energy dynamics in extended parameter space. *Physical Review D*, 96(2):023523, 2017.
- [64] Eleonora Di Valentino, Alessandro Melchiorri, and Olga Mena. Can interacting dark energy solve the h_0 tension? *Physical Review D*, 96(4):043503, 2017.
- [65] P. Keshav MV and K. Arun. Interacting dark energy and its implications for unified dark sector. *International Journal of Theoretical Physics*, 63:265, 2024.
- [66] Eleonora Di Valentino, Alessandro Melchiorri, Olga Mena, and Sunny Vagnozzi. Nonminimal dark sector physics and cosmological tensions. *Physical Review D*, 101(6):063502, 2020.
- [67] David Ruelle. Strange attractors. *Turbulence, Strange Attractors, and Chaos*, 16:195, 1995.
- [68] John Guckenheimer and Philip Holmes. *Nonlinear oscillations, dynamical systems, and bifurcations of vector fields*. Springer Science & Business Media, 2013.

- [69] Dumitru M Ghilencea. Spontaneous breaking of weyl quadratic gravity to einstein action and higgs potential. *Journal of High Energy Physics*, 2019(3):1–15, 2019.
- [70] D Boyanovsky, D Cormier, HJ De Vega, R Holman, and S Prem Kumar. Nonperturbative quantum dynamics of a new inflation model. *Physical Review D*, 57(4):2166, 1998.
- [71] Markus Heyl. Dynamical quantum phase transitions: a review. *Reports on Progress in Physics*, 81(5):054001, 2018.
- [72] Matthias Vojta. Quantum phase transitions. *Reports on Progress in Physics*, 66(12):2069–2110, 2003.
- [73] Christian Armendariz-Picon and Eugene A Lim. Haloes of k-essence. *Journal of Cosmology and Astroparticle Physics*, 2005(08):007–007, 2005.
- [74] Eric V Linder. The dynamics of quintessence, the quintessence of dynamics. *General Relativity and Gravitation*, 40(2):329–356, 2008.
- [75] Yashar Akrami, Misao Sasaki, Adam R Solomon, and Valeri Vardanyan. Multi-field dark energy: Cosmic acceleration on a steep potential. *Physics Letters B*, 819:136427, 2021.
- [76] MV Pradosh Keshav and Arun Kenath. Loop-corrected scalar potentials and late-time acceleration in f (r) gravity. *The European Physical Journal C*, 85(9):990, 2025.
- [77] Sidney Coleman and Erick Weinberg. Radiative corrections as the origin of spontaneous symmetry breaking. *Physical Review D*, 7(6):1888, 1973.
- [78] Michael S Turner. Windows on the axion. *Physics Reports*, 197(2):67–97, 1990.
- [79] Michael Dine, Willy Fischler, and Mark Srednicki. A simple solution to the strong cp problem with a harmless axion. *Physics letters B*, 104(3):199–202, 1981.
- [80] Diego Blas, Julien Lesgourgues, and Thomas Tram. The cosmic linear anisotropy solving system (class). part ii: Approximation schemes. *Journal of Cosmology and Astroparticle Physics*, 2011(07):034–034, 2011.
- [81] Dillon Brout, Georgie Taylor, Dan Scolnic, Charlotte M Wood, Benjamin M Rose, Maria Vincenzi, Arianna Dwomoh, Christopher Lidman, Adam Riess, Noor Ali, et al. The pantheon+ analysis: Supercal-fragilistic cross calibration, retrained salt2 light-curve model, and calibration systematic uncertainty. *The Astrophysical Journal*, 938(2):111, 2022.
- [82] Daniel Foreman-Mackey, David W Hogg, Dustin Lang, and Jonathan Goodman. emcee: the mcmc hammer. *Publications of the Astronomical Society of the Pacific*, 125(925):306–312, 2013.
- [83] Roberto Scaramella, J Amiaux, Y Mellier, Carlo Burigana, CS Carvalho, J-C Cuillandre, A Da Silva, A Derosa, J Dinis, E Maiorano, et al. Euclid preparation-i. the euclid wide survey. *Astronomy & Astrophysics*, 662:A112, 2022.
- [84] Yun Wang, Zhongxu Zhai, Anahita Alavi, Elena Massara, Alice Pisani, Andrew Benson, Christopher M Hirata, Lado Samushia, David H Weinberg, James Colbert, et al. The high latitude spectroscopic survey on the nancy grace roman space telescope. *The Astrophysical Journal*, 928(1):1, 2022.
- [85] Ziad Sakr and Jessica N López-Sánchez. Forecast on the generalised dark matter properties from a euclid-like survey. *arXiv preprint arXiv:2601.16943*, 2026.
- [86] Shinji Tsujikawa. Crossing the phantom divide in scalar-tensor and vector-tensor theories. *Physical Review D*, 113(4):L041301, 2026.

- [87] Luca Amendola. Scaling solutions in general nonminimal coupling theories. *Physical Review D*, 60(4):043501, 1999.
- [88] Luca Amendola. Perturbations in a coupled scalar field cosmology. *Monthly Notices of the Royal Astronomical Society*, 312(3):521–530, 2000.